Dissolved silicon isotope dynamics in large river estuaries

Zhouling Zhang[1], Zhimian Cao[1]*, Patricia Grasse[2], Minhan Dai[1], Lei Gao[3], Henning Kuhnert[4], Martha Gledhill[2], Cristiano M. Chiessi[5], Kristin Doering[2,6], Martin Frank[2]

[1]State Key Laboratory of Marine Environmental Science and College of Ocean and Earth Sciences, Xiamen University, Xiamen 361102, China

[2]GEOMAR Helmholtz Center for Ocean Research Kiel, Kiel 24148, Germany

[3]State Key Laboratory of Estuarine and Coastal Research, East China Normal University, Shanghai 20062, China

[4]MARUM Center for Marine Environmental Sciences, University of Bremen, Bremen 28359, Germany

[5]School of Arts, Sciences and Humanities, University of São Paulo, São Paulo 03828-000, Brazil

[6]Department of Oceanography, Dalhousie University, Halifax, NS B3H 4R2, Canada

*Corresponding author:

Dr. Zhimian Cao

State Key Laboratory of Marine Environmental Science

Xiamen University

Xiang'an District

Xiamen 361102, China

Phone: +86-592-2186029

Fax: +86-592-2184101

E-mail: zmcao@xmu.edu.cn

Abstract

Estuarine systems are of key importance for the riverine input of silicon (Si) to the ocean, which is a limiting factor of diatom productivity in coastal areas. This study presents a field dataset of surface dissolved Si isotopic compositions ($\delta^{30}Si_{Si(OH)4}$) obtained in the estuaries of three of the world's largest rivers, the Amazon (ARE), Yangtze (YRE), and Pearl (PRE), which cover different climate zones. While $\delta^{30}Si_{Si(OH)4}$ behaved conservatively in the YRE and PRE supporting a dominant control by water mass mixing, significantly increased $\delta^{30}Si_{Si(OH)4}$ signatures due to diatom utilization of $Si(OH)_4$ were observed in the ARE and reflected a Si isotopic enrichment factor $^{30}\varepsilon$ of −1.0±0.4‰ (Rayleigh model) or −1.6±0.4‰ (steady state model). In addition, seasonal variability of Si isotope behavior in the YRE was observed by comparison to previous work and most likely resulted from changes in water residence time, temperature, and light level. Based on the $^{30}\varepsilon$ value obtained for the ARE, we estimate that the global average $\delta^{30}Si_{Si(OH)4}$ entering the ocean is 0.2-0.3‰ higher than that of the rivers due to Si retention in estuaries. This systematic modification of riverine Si isotopic compositions during estuarine mixing, as well as the seasonality of Si isotope dynamics in single estuaries, needs to be taken into account for better constraining the role of large river estuaries in the oceanic Si cycle.

1. INTRODUCTION

The land-to-ocean silicon (Si) flux, mainly occurring via riverine discharge, is of great importance because it strongly stimulates diatom growth in coastal oceans, thereby significantly contributing to global carbon fixation (Laruelle et al., 2009; Treguer and De La Rocha, 2013; Frings et al., 2016). Estuaries, situated between freshwater and marine environments, are key components of the land-ocean aquatic continuum and are highly complex environments with distinct patterns of salinity, pH, nutrients, and turbidity (e.g., Edmond et al., 1985; Nelson and Dortch, 1996; Cai et al., 2004). Estuarine mixing alters the distributions of dissolved and particulate materials delivered by rivers through, for example, adsorption-desorption onto particles (e.g., Nguyen et al., 2019), mineral precipitation and dissolution (e.g., Singurindy et al., 2004), and uptake by organisms (e.g., DeMaster et al., 1996). Dissolved silicate ($Si(OH)_4$) concentrations often deviate from conservative mixing behavior between river water and seawater in estuaries, which can be induced by both biotic and abiotic processes (e.g., Carbonnel et al., 2013; Treguer and De La Rocha, 2013). Diatoms incorporate $Si(OH)_4$ into their frustules during growth and export biogenic silica (bSi) to the sediments, thereby removing Si from the dissolved pool (e.g., DeMaster, 1981; Conley and Malone, 1992). In the sediments, diagenetic reactions via dissolution of bSi and formation of authigenic silicate minerals (i.e., reverse weathering) help to further preserve Si (e.g., Michalopoulos and Aller, 1995, 2004; Rahman et al., 2017). In contrast, the dissolution of fluvial amorphous silica (ASi) adds Si to estuarine environments, which has been demonstrated in both laboratory experiments (e.g., Oelkers et al., 2011; Jones et al., 2012) and field studies (e.g., Pastuszak et al., 2008; Carbonnel et al., 2013; Lehtimäki et al., 2013). Furthermore, anthropogenic activities may decrease (such as damming; Conley, 2002; Hughes et al., 2012) or increase (such as deforestation and climate warming; Conley et al., 2008; Laruelle et

al., 2009) $Si(OH)_4$ concentrations and impact the riverine Si flux to the estuaries.

Tropical and subtropical rivers are the major contributors of riverine Si input to the ocean (Zhang et al., 1999; Beusen et al., 2009). Taking into account the strong climatic control on the weathering regime and intensity, processes affecting Si in estuaries associated with changing climate zones are of particular interest. In addition, large river estuaries with high water and sediment discharge commonly exhibit not only high turbidity and complex physical circulation but also significant seasonal variability in nutrient dynamics and phytoplankton bloom development (DeMaster and Pope, 1996).

Despite their potential significance for global Si cycling, our knowledge of the role of large river estuaries is still limited (Weiss et al., 2015; Frings et al., 2016; Sutton et al., 2018). One reason is that the Si concentration distributions only partially reveal Si dynamics. Over the past two decades, the stable isotopic composition of Si ($\delta^{30}Si$) has been developed as a powerful tool for identifying Si sources and tracking Si biogeochemical processes over various temporal and spatial scales (e.g., Varela et al., 2004; Zhang et al., 2019). In comparison to extensive studies conducted in rivers, lakes, and the ocean (Sutton et al., 2018, and references therein), information on factors controlling dissolved Si isotope compositions ($\delta^{30}Si_{Si(OH)4}$) in estuaries is sparse and data have so far only been reported for four estuaries worldwide (Hughes et al., 2012; Delvaux et al., 2013; Weiss et al., 2015; Zhang et al., 2015). In the tropical Tana River Estuary, $Si(OH)_4$ concentrations decrease linearly with increasing salinity, whereas $\delta^{30}Si_{Si(OH)4}$ signatures remain stable due to the absence of processes fractionating Si isotopes (Hughes et al., 2012). A notable increase of $\delta^{30}Si_{Si(OH)4}$ has been observed to occur during diatom growth in the tidal freshwater zone of both the Scheldt River (Delvaux et al., 2013) and the Elbe River estuaries (Weiss et al., 2015). Heavier $\delta^{30}Si_{Si(OH)4}$ signatures induced by biological utilization also occur at high salinities

in the Yangtze River Estuary in summer (Zhang et al., 2015). Given the large importance of estuaries, integrated efforts are necessary for the development of a more comprehensive understanding of the global Si cycle (Sutton et al., 2018).

In this study, we investigate for the first time surface water $\delta^{30}Si_{Si(OH)4}$ distributions and their controlling processes in the estuaries of three of the world's largest rivers, namely the Amazon River (1st) in the tropical zone, the Yangtze River (or Changjiang, 5th) in the temperate zone and the Pearl River (or Zhujiang, 13th) in the subtropical zone, including both the embayment and adjacent shelf (Fig. 1). The relationship between $\delta^{30}Si_{Si(OH)4}$ and salinity is investigated in each estuarine system to distinguish between chemical and biological fractionation effects and conservative mixing. Given that these rivers represent more than one fifth of the global freshwater discharge to the ocean, their Si isotope dynamics will shed new light on the importance of estuarine processes in the oceanic Si cycle.

2. MATERIALS AND METHODS

2.1. Study area

Amazon River Estuary (ARE). The Amazon River, covering over 20° of latitude and extending longitudinally across 3,000 km, is the largest river in the world (Nittrouer and DeMaster, 1996). It discharges 5.8×10^{12} m^3 yr^{-1} of freshwater with peak flow in June and minimum flow in November, which is approximately 20% of the global river water discharge (Meade et al., 1985; DeMaster and Pope, 1996). It also delivers 1.1-1.3$\times10^9$ ton yr^{-1} of suspended sediments to its lower reaches, contributing up to 7% of the global riverine sediment input to the ocean (Meade et al., 1985). The ARE is located in the low-latitude tropical zone where the freshwater plume from the river interacts with the North Brazil Current and is transported to the northwest (Milliman and Boyle, 1975; Johns et al., 1998). It is not strongly anthropogenically influenced and thus relatively low in nutrient and

cation contents (DeMaster and Pope, 1996), though recent studies have shown human-induced perturbations in the southern and eastern portions of the Amazon River drainage basin (Davidson et al., 2012; Latrubesse et al., 2017). The Si input from the ARE is the major source of $Si(OH)_4$ to the adjacent shelf with a smaller contribution from shoreward advection of offshore waters (Michalopoulos and Aller, 2004). Primary productivity, dominantly driven by diatoms (DeMaster et al., 1996), is highest in an intermediate zone between the turbid nutrient-rich Amazon plume waters inshore and the clear nutrient-poor marine surface waters offshore (Smith and Demaster, 1996).

Yangtze River Estuary (YRE). After a total of 6,300 km of eastward flow to the East China Sea, the Yangtze River supplies 9.2×10^{11} m^3 yr^{-1} of freshwater and 4.7×10^8 ton yr^{-1} of sediments to the ocean (Wang et al., 2015). More than 70% of the freshwater discharge occurs in the flood season (May-October) (Zhang et al., 2015). The YRE, located in the temperate climate zone (e.g., Patra et al., 2012), is characterized by high nutrient contents due to anthropogenic eutrophication and high cation contents due to high weathering rates. The riverine fluxes of dissolved inorganic nitrogen (DIN) and dissolved inorganic phosphate (DIP) are estimated to be 9.50×10^5 and 2.63×10^4 ton yr^{-1} (Liu et al., 2009). The $Si(OH)_4$ flux has decreased sharply after the construction of large reservoirs in the Yangtze River drainage basin, from 2.72×10^5 in the 1960s to 2.13×10^5 ton yr^{-1} in the 1980s. In 2002, ~13% of the total $Si(OH)_4$ flux was fixed by phytoplankton within 162 big reservoirs before entering into the East China Sea (Li et al., 2007). On the other hand, Gao et al. (2012) pointed out no significant changing trend of $Si(OH)_4$ concentrations and fluxes near the YRE mouth since 1960s, suggesting that the long-term variability of $Si(OH)_4$ loads by the Yangtze River needs further investigation. Nevertheless, application of chemical fertilizers has increased N and P fluxes and enhanced N:Si and P:Si ratios since the 1980s. This has significantly

increased the abundance of non-siliceous algae over diatoms off the YRE (Li et al., 2007).

Pearl River Estuary (PRE). The Pearl River drains an area of 452,000 km^2 and reaches the South China Sea after 2,214 km southward flow. It is a large subtropical river located in a highly populated and industrialized area (e.g., Zhang et al., 1999). It discharges 1.6×10^{11} m^3 yr^{-1} of freshwater and 8.5×10^7 ton yr^{-1} of sediments into the South China Sea via three estuaries, among which the Lingdingyang, known as the PRE, receives 50-55% of the freshwater discharge (Harrison et al., 2008). Approximately 80% of the freshwater discharge occurs in the wet season (April-September) and only 20% in the dry season (October-March) (Zhang et al., 1999; Cai et al., 2004). With the rapid economic development and urbanization of the upper PRE, anthropogenic loads of nutrients have dramatically increased in the last few decades. From 2001 to 2008, for example, the total ammonium discharge from Guangdong Province increased from 9.0×10^4 to 12.2×10^4 ton (He et al., 2014). However, the phytoplankton biomass is not as high as one would expect from the high level of nutrients, probably due to dilution by river discharge, estuarine circulation, and/or vertical mixing (Harrison et al., 2008). Moreover, diatom blooms in the PRE are seasonally highly variable and confined to spatially limited locations associated with suitable coupled physical-biological conditions (Lu and Gan, 2015).

2.2. Sampling and analyses

2.2.1. Sampling

Sampling in the mixing zone of the ARE was carried out during R/V *Meteor* Cruise M147 (Amazon-GEOTRACES) in May 2018, when the monthly discharge was 6.1×10^{11} m^3 (data from Óbidos observation station; http://www.ore-hybam.org). The samples were taken along a section covering the complete salinity gradient between the riverine endmember and open seawater. The ship's conventional stainless steel Conductivity-Temperature-Depth (CTD) rosette equipped with

24-Niskin bottles was only briefly submerged at the surface in an effort to avoid vertical mixing and allow sampling of the undisturbed uppermost freshwater layer. Water for $\delta^{30}Si_{Si(OH)4}$ analyses was sampled into 20 L cubitainers and filtered through 0.45 μm Nucleopore filters within a few hours after collection. Samples at stations M147_55-F (surface salinity of 35.0) and M147_56-F (surface salinity of 30.0) on the shelf (Table 1) were taken with a towed fish and treated the same way. All samples were subsequently acidified to pH~2 with concentrated ultrapure HCl to prevent adsorption of metals to the walls of the bottles. Surface water samples were also collected for analyses of nutrients (DIN (nitrate plus nitrite), DIP, and $Si(OH)_4$) and chlorophyll a (Chl-a). In addition to this cruise to the ARE, $Si(OH)_4$ concentration and $\delta^{30}Si_{Si(OH)4}$ data were also collected at a single upstream station at zero salinity in November 2013 and at other stations on the shelf in February 2012 (see Text A2 for details).

Sampling in the YRE was carried out in March 2015, when the monthly discharge was 5.4×10^{10} m^3 (data from Datong observation station; http://www.mwr.gov.cn). Sampling in the PRE was carried out in August 2012, when the monthly discharge was 2.7×10^{10} m^3 (data from Wuzhou observation station; http://www.mwr.gov.cn). In both estuaries, ~150 ml of surface water was collected with Niskin bottles attached to a rosette sampler and immediately filtered through nitrocellulose acetate filters (0.45 μm pore size and 47 mm diameter) into acid pre-cleaned polyethylene bottles for $\delta^{30}Si_{Si(OH)4}$ analyses. Samples were subsequently acidified to pH~2 with distilled concentrated HCl (0.1% v/v) and stored at room temperature in the dark until analysis in the laboratory. Surface water samples were also collected in the YRE and PRE for analyses of nutrients (DIN (nitrate plus nitrite), DIP, and $Si(OH)_4$), Chl-a, and total suspended matter (TSM).

2.2.2. Si isotope analyses

Si isotopic compositions were measured on a Nu Plasma HR multi-collector inductively coupled plasma mass spectrometry (MC-ICP-MS; Nu Instruments™, Wrexham, UK) at GEOMAR, Kiel and are reported in ‰ deviations from the international Si standard NIST Reference Material 8546 (or NBS28) ($\delta^{30}Si=[(^{30}Si/^{28}Si)_{sample}/(^{30}Si/^{28}Si)_{standard}-1]\times1000$).

(1) Sample treatment

$Si(OH)_4$ in all ARE samples collected in May 2018 was pre-concentrated and separated from the major matrix elements using a two-step brucite coprecipitation technique (Reynolds et al., 2006), with low-salinity samples pre-treated with Mg^{2+} addition (Zhang et al., 2015), which was further purified using cation-exchange chromatography (Georg et al., 2006). For the YRE and PRE, $Si(OH)_4$ in samples with low concentrations (<40.0 μmol L^{-1}; Table 1) was pre-concentrated via brucite coprecipitation before cation-exchange chromatography, while $Si(OH)_4$ in other samples with high concentrations (>40.0 μmol L^{-1}; Table 1) was directly purified using cation-exchange chromatography given that their $Si(OH)_4$ content was sufficiently high for measurement on the MC-ICP-MS. Recent work has shown that Si isotope measurements on MC-ICP-MS are susceptible to anions or organic compounds in the matrix (e.g., van den Boorn et al., 2009; Hughes et al., 2011). However, the Nu Plasma HR MC-ICP-MS at GEOMAR is less sensitive to these matrices. Ehlert et al. (2016) did tests in order to check the matrix effect from anions and dissolved organic matter on pore-water Si isotopic compositions using the same instrument, which showed no significant matrix effects.

(2) Mass spectrometry

Each purified sample solution was analyzed three to four times in a single measurement session using a standard-sample-standard bracketing technique, resulting in sample reproducibilities between ±0.03 and ±0.31‰ (2 standard deviations, $2SD_{bracketing}$; Table 1). For

most of the samples, purification and determination of isotopic compositions were repeated on two or three days and the duplicate measurements indicate very good reproducibilities between ±0.01 and ±0.23‰ ($2SD_{repeated}$; Table 1).

Repeated measurements of the standard reference materials IRMM-018 and Big Batch gave average $\delta^{30}Si$ values of −1.45±0.15‰ ($2SD_{repeated}$, n=5) and −10.70±0.14‰ ($2SD_{repeated}$, n=5) during measurements of the ARE samples collected in May 2018, and of −1.39±0.15‰ ($2SD_{repeated}$, n=7) and −10.67±0.19‰ ($2SD_{repeated}$, n=8) during measurements of the YRE and PRE samples. All these values are in good agreement with those obtained during a previous interlaboratory comparison (Reynolds et al., 2007). An average $\delta^{30}Si_{Si(OH)4}$ value of 1.79±0.29‰ ($2SD_{repeated}$, n=3; with coprecipitation) for the seawater standard $ALOHA_{300}$ was obtained during running the ARE samples. Average $\delta^{30}Si_{Si(OH)4}$ values of 1.27±0.17‰ ($2SD_{repeated}$, n=9; with coprecipitation) and 1.41±0.18‰ ($2SD_{repeated}$, n=8; without coprecipitation) for the seawater standard $ALOHA_{1000}$ were obtained during running the ARE samples and the YRE and PRE samples, respectively. These values are within analytical error identical to or slightly higher than the consensus values (1.68±0.35‰ for pre-concentrated $ALOHA_{300}$ and 1.24±0.20‰ for pre-concentrated $ALOHA_{1000}$) obtained in the GEOTRACES inter-calibration study (Grasse et al., 2017). The long-term external reproducibility for the replicate measurements of an in-house seawater matrix standard was ±0.20‰ (2SD, n=16), which represents the error bars of the majority of the field $\delta^{30}Si_{Si(OH)4}$ data of our study. For few samples with $2SD_{repeated}$ larger than ±0.20‰, the $2SD_{repeated}$ was used as error bars of $\delta^{30}Si_{Si(OH)4}$ (Figs. 3b, d, f, A4b, d, A5, and A6). We contend that there might be a tendency towards slightly heavier $\delta^{30}Si_{Si(OH)4}$ for samples without than with coprecipitation and further comparisons should be conducted carefully. However, the offset of 0.14‰, as shown by our

measurements of $ALOHA_{1000}$ using both pre-treatments, is within the long-term external reproducibility of ±0.20‰. More information on data quality can be found in Text A1.

2.2.3. Analyses of other parameters

In the ARE, salinities of the discrete surface water samples taken with the towed fish were determined with a hand-held conductivity meter (WTW LF330) and those taken with the CTD rosette were determined with a hand-held conductivity meter (WTW 3110) and corresponding probe Tetracon 325 to ensure comparability of all data. Nutrient concentrations in the water samples were analyzed following classical colorimetric methods, using a SEAL QuAAtro continuous flow Auto-Analyzer (Hydes et al., 2010). Chl-a concentrations were determined after extraction into cold (−20°C) acetone by high performance liquid chromatography with spectrophotometric detection (Van Heukelem and Thomas, 2001). In the YRE and PRE, salinities of surface water samples were determined with a SBE25 CTD (Sea-Bird) attached to a rosette sampler and was compared with salinity of discrete samples measured by a Multi 340i multi-parameter meter (WTW). Nutrient concentrations in the water samples were analyzed using a Nutrient Auto-Analyzer (SKALAR San^{plus} System) for the YRE and a Technicon AA3 Auto-Analyzer (Bran-Luebbe, GmbH) for the PRE. The precisions for DIN, DIP, and $Si(OH)_4$ concentrations were ±1%, ±2%, and ±3%, respectively (1SD; Du et al., 2013). Chl-a concentrations were determined using a Turner fluorometer after extraction of the membrane samples with 90% acetone (He et al., 2014). TSM concentrations were determined by drying in an oven at 50°C and weighing the quartz microfiber membranes used for filtering (Zhai et al., 2017).

2.3. Si isotope fractionation model

Si isotope fractionation during $Si(OH)_4$ consumption can be described using either a Rayleigh or a steady state model (Cao et al., 2012, and references therein). The Rayleigh model describes a

closed system without further $Si(OH)_4$ input from external sources:

$$\delta^{30}Si_{Si(OH)4\_obs} = \delta^{30}Si_{Si(OH)4\_ini} + {}^{30}\varepsilon \times \ln f \quad (1)$$

$$f = \frac{[Si(OH)_4]_{obs}}{[Si(OH)_4]_{ini}} \quad (2)$$

The subscript "obs" and "ini" denote measured $\delta^{30}Si_{Si(OH)4}$ and $Si(OH)_4$ values and initial $\delta^{30}Si_{Si(OH)4}$ and $Si(OH)_4$ values, respectively, with the latter being equal to conservative $\delta^{30}Si_{Si(OH)4}$ and $Si(OH)_4$ values predicted by a two-endmember mixing model ($\delta^{30}Si_{Si(OH)4\_con}$ and $[Si(OH)_4]_{con}$; Eqs. A3 and A4; Text A3). The term *f* indicates the fraction of remaining dissolved $Si(OH)_4$ in solution relative to the initial concentration. The isotopic enrichment factor ${}^{30}\varepsilon$ is thus estimated as:

$${}^{30}\varepsilon = \frac{\delta^{30}Si_{Si(OH)4\_obs} - \delta^{30}Si_{Si(OH)4\_ini}}{\ln f} = \frac{\delta^{30}Si_{Si(OH)4\_obs} - \delta^{30}Si_{Si(OH)4\_ini}}{\ln \frac{[Si(OH)_4]_{obs}}{[Si(OH)_4]_{ini}}} \quad (3)$$

In contrast, the steady state model describes an open system with a continuous supply of $Si(OH)_4$ from external sources:

$$\delta^{30}Si_{Si(OH)4\_obs} = \delta^{30}Si_{Si(OH)4\_ini} - {}^{30}\varepsilon \times (1-f) \quad (4)$$

In this case, ${}^{30}\varepsilon$ is calculated as:

$${}^{30}\varepsilon = \frac{\delta^{30}Si_{Si(OH)4\_ini} - \delta^{30}Si_{Si(OH)4\_obs}}{1-f} = \frac{\delta^{30}Si_{Si(OH)4\_ini} - \delta^{30}Si_{Si(OH)4\_obs}}{1-\frac{[Si(OH)_4]_{obs}}{[Si(OH)_4]_{ini}}} \quad (5)$$

By combining the two-endmember mixing model (Text A3) and the Si isotope fractionation models, we are able to distinguish chemical or biological effects on Si concentrations and isotopic compositions from pure conservative mixing.

3. RESULTS

3.1. Surface distribution of salinity, $Si(OH)_4$, and $\delta^{30}Si_{Si(OH)4}$

In all three estuaries, surface salinities generally increased from the upper reaches or the mouth (<1.0) to the adjacent shelf (Fig. 2a, e, j), reflecting estuarine mixing between the fresh river waters and the saline seawaters. Salinities at the outermost offshore stations were 35.0, 34.0, and 31.1 for the ARE, YRE, and PRE (Table 1), suggesting the dominance of oceanic shelf water in the ARE and YRE and the still significant influence of river plume water in the PRE during the high discharge season in August.

Surface $Si(OH)_4$ concentrations generally decreased from the upper estuaries to the shelf (Fig. 2b, f, k) reflecting high riverine input of nutrients to the coastal shelf areas. The $Si(OH)_4$ concentrations (0.6-150.2 μmol L^{-1} for the ARE, 9.2-106.3 μmol L^{-1} for the YRE, and 14.9-166.7 μmol L^{-1} for the PRE) are overall comparable between the three estuaries (and adjacent shelf areas) with slightly higher values observed in the upper PRE near zero salinity. The $\delta^{30}Si_{Si(OH)4}$ signatures were significantly heavier in surface seawaters than in the river waters (3.0 vs. 1.2‰ for the ARE, 2.6 vs. 1.7‰ for the YRE, and 1.8 vs. 1.3‰ for the PRE; Fig. 2c, g, l; Table 1), with the largest increase observed in the ARE. The highest surface $\delta^{30}Si_{Si(OH)4}$ value at the outermost offshore station in the PRE is lower than those of the ARE and YRE, largely due to the still higher proportion of the low-$\delta^{30}Si_{Si(OH)4}$ river plume water indicated by its lower salinity. Note that $\delta^{30}Si_{Si(OH)4}$ was not measured at salinity of 35.0 in the ARE due to the extremely low amount of dissolved Si in the surface seawater, and 3.0‰ reflects the $\delta^{30}Si_{Si(OH)4}$ value measured at a salinity of 30.0.

3.2. Surface distribution of TSM and Chl-a

The TSM concentrations ranged from 0 to 120 mg L^{-1} in the YRE with the maximum concentrations observed at salinities of 7.5 to 16.0 (Fig. 2h), whereas they were significantly lower in the PRE with a maximum of up to 60 mg L^{-1} observed at a salinity of 6.5 (Fig. 2m). This

indicates the development of a turbidity maximum zone (TMZ, TSM >10 mg L^{-1}) at low salinities directly following the freshwater regions in both estuaries. Diatom growth is suppressed in the TMZ of estuaries due to light limitation (Edmond et al., 1985). TSM concentrations were much higher than 10 mg L^{-1} over the entire salinity range in the YRE (Fig. 2h), as well as at most stations with salinities <11.8 in the PRE (Fig. 2m). Unfortunately, no TSM data were collected during cruise M147 to the ARE. Previous studies have demonstrated, however, that the TMZ occurs at salinities below 17.0 (DeMaster and Pope, 1996).

In the ARE, Chl-a concentrations were lower than 3 μg L^{-1} in the freshwater zone with salinities <4.0 and increased to a maximum of 14 μg L^{-1} at a salinity of 15.0. Chl-a remained at high levels in the mixing zone at mid-salinities from 20.0 to 28.0 (Fig. 2d), suggesting abundant phytoplankton growth downstream of the TMZ. Consistent with the high turbidity, Chl-a concentrations were overall lower than 3 μg L^{-1} in the YRE (Fig. 2i), indicating largely reduced phytoplankton growth during the sampling period. In the PRE, Chl-a concentrations were distinctly elevated in the upper stream at salinities <1.0 and the highest value of 11 μg L^{-1} was observed at the freshest upstream station (Fig. 2n). This high Chl-a region clearly located upstream of the TMZ was likely induced by transport of freshwater algae from the drainage basin (He et al., 2014) and/or in situ biological production due to the high nutrient content and relatively low TSM (Anderson, 1986). Chl-a concentrations decreased rapidly in the TMZ of the PRE, but then higher Chl-a (>4 μg L^{-1}) were subsequently observed again at salinities of 16.5 and 24.0 (Fig. 2n), indicating enhanced phytoplankton growth at mid-salinities with reduced TSM.

Overall, in all three estuaries, phytoplankton growth generally increased towards the outer parts of the estuaries, where the decrease in nutrient levels is compensated for by the increase in water transparency and thus light availability.

4. DISCUSSION

4.1. Differences in $\delta^{30}Si_{Si(OH)4}$ signatures of river water endmembers between estuaries

The $Si(OH)_4$ concentration and $\delta^{30}Si_{Si(OH)4}$ value at zero salinity of the ARE amounted to 150.2 μmol L^{-1} and 1.2±0.2‰, respectively, in May 2018 (field measurements at station M147_66-1; Table 1), and reached 125.3 μmol L^{-1} and 1.3±0.2‰, respectively, in November 2013 (field measurements at station River; Table A1). Therefore, our data show a consistent $\delta^{30}Si_{Si(OH)4}$ composition of the river water endmember despite differing $Si(OH)_4$ concentrations, sampling locations, and sampling periods. A $\delta^{30}Si_{Si(OH)4}$ signature of 1.8±0.2‰ ($Si(OH)_4$ concentrations of 102.7 μmol L^{-1}) for the river water endmember in the YRE (the averages of field measurements at stations C4, C5, C6, and C7) is within error consistent with 1.6‰ provided by Zhang et al. (2015). Our $\delta^{30}Si_{Si(OH)4}$ value of 1.4±0.2‰ ($Si(OH)_4$ concentrations of 143.8 μmol L^{-1}) for the river water endmember in the PRE (the averages of field measurements at stations P04, A01, A02, A03, and A04) is comparable to that of the ARE but lighter than that of the YRE. Such differences in $\delta^{30}Si_{Si(OH)4}$ signatures of various river water endmembers most likely resulted from stronger fractionation in the Yangtze River catchment induced by a combined effect of relatively high weathering intensity, biological utilization, and anthropogenic activities (Text A4; Zhang et al., 2003; Li et al., 2007; Ding et al., 2014; Frings et al., 2016). Note that the uncertainties of $\delta^{30}Si_{Si(OH)4}$ values for the river water endmembers, based on the selected field measurements, derived either from the propagation of their analytical errors (i.e., the long-term external reproducibility of ±0.20‰ or $2SD_{repeated}$ if they are larger than ±0.2‰) or from the standard deviation of all field measured $\delta^{30}Si_{Si(OH)4}$ values, which are 0.2 or 0.2‰ in the ARE, 0.1 or 0.04‰ in the YRE, and 0.1 or 0.04‰ in the PRE, respectively. We thus conservatively use the long-term external reproducibility of 0.2‰ for the Si isotope analyses as the uncertainties of $\delta^{30}Si_{Si(OH)4}$ endmember values.

4.2. Si isotope dynamics during estuarine mixing

The relationship between the dissolved phase and salinity is widely used to interpret the biogeochemical behavior of a given element during estuarine mixing between river water and seawater. In this study, the water mass compositions at near zero salinity and at the highest salinity are selected as the two endmembers in each estuary (Fig. 3). Estimations of $Si(OH)_4$ concentrations and $\delta^{30}Si_{Si(OH)4}$ values for the river water endmember are introduced in subsection 4.1. In the ARE, salinity and $Si(OH)_4$ concentration for the seawater endmember were 35.0 and 0.6 μmol L^{-1}, respectively, based on the field measurements at station M147_55-F (Table 1). $\delta^{30}Si_{Si(OH)4}$ at this station was estimated to be 3.2±0.3‰ using a linear relationship between $\delta^{30}Si_{Si(OH)4}$ and $\ln(Si(OH)_4)$ based on available data in the ARE in May 2018 ($\delta^{30}Si_{Si(OH)4}=(3.01\pm0.29)-(0.31\pm0.08)\times\ln(Si(OH)_4)$, $R^2=0.81$; Fig. A5), with the uncertainty propagated from that of the intercept and slope. In the YRE, salinity, $Si(OH)_4$ concentration, and $\delta^{30}Si_{Si(OH)4}$ values for the seawater endmember were 33.8, 10.3 μmol L^{-1}, and 2.4±0.2‰ based on the averages of field measurements at stations A06-9 and A06-11 (Table 1). In the PRE, salinity, $Si(OH)_4$ concentration, and $\delta^{30}Si_{Si(OH)4}$ values for the seawater endmember were 31.1, 14.9 μmol L^{-1}, and 1.7±0.2‰ based on the field measurements at station F415 (Table 1). A sensitivity test using open ocean seawater endmembers is carried out, which shows that our selection and estimation of seawater endmembers above are valid (Text A5 and Fig. A6). Note that here, we conservatively use the long-term reproducibility of 0.2‰ to represent the uncertainties of $\delta^{30}Si_{Si(OH)4}$ endmember values for predicting the conservative estuarine mixing, except for the ARE seawater endmember, the uncertainty of which is larger at 0.3‰ (Figs. 3 and A6). Clearly, Si biogeochemistry differs between the three estuaries when comparing field measurements along the salinity gradient with the predicted two-endmember conservative mixing following Eqs. A1-A4

(Fig. 3).

4.2.1. Amazon River Estuary: biological fractionation during diatom growth

The $Si(OH)_4$ concentration of 150.2 μmol L^{-1} at zero salinity in the ARE is close to the annual average value of 163 μmol L^{-1} observed at Óbidos observation station (Moquet et al., 2016), suggesting that our zero salinity sample represents a realistic river water endmember. Significant removal of $Si(OH)_4$ corresponding to elevated $\delta^{30}Si_{Si(OH)4}$ that cannot be explained by mixing is observed over the entire salinity range (Fig. 3a, b), reflecting preferential utilization of $Si(OH)_4$ with lighter Si isotopic composition. Both DIN (Fig. 4a) and DIP (Fig. 4b) generally show significant removal at salinities >10.0 in the ARE, indicating strong nutrient uptake by phytoplankton as evidenced by high Chl-a concentrations (up to 14 μg L^{-1}; Fig. 2d). Applying Eqs. A1-A4, we obtain the expected initial $Si(OH)_4$ and $\delta^{30}Si_{Si(OH)4}$ values for every single measurement within this salinity range. Based on these data, calculated $Si(OH)_4$ consumption (1-*f*; Eqs. 2 and A3) ranged from 6% at low salinity of 4.0 to 44±7% (n=6) at mid-salinities of 6.7-27.3 and to 94% at high salinity of 30.0 (Table A2). This is consistent with an overall increasing trend of $Si(OH)_4$ depletion from the inner to the outer shelf (DeMaster et al., 1996). The average isotopic enrichment factor $^{30}\varepsilon$ is estimated to be −1.0±0.4‰ following the Rayleigh model (Eq. 3) or −1.6±0.4‰ following the steady state model (Eq. 5).

Culture experiments (De La Rocha et al., 1997; Milligan et al., 2004; Sutton et al., 2013; Meyerink et al., 2017; Meyerink et al., 2019) have discovered a range of $^{30}\varepsilon$ (−0.54 to −2.09 ‰) with an average of −1.1‰ during $Si(OH)_4$ utilization by diatoms. Field studies (e.g., Reynolds et al., 2006; Beucher et al., 2008; Fripiat et al., 2011; Cao et al., 2012, 2015) have validated this value in different oceanic systems. Our estimates in the ARE, assuming either a closed or an open system, agree well with this consensus value, supporting a major role of diatoms in controlling the Si

isotope signatures. Previous studies have shown that diatoms are the predominant primary producers on the Amazon shelf, which control $Si(OH)_4$ distributions and removal (e.g. DeMaster et al., 1996), as well as the corresponding Si isotope fractionation. However, it is difficult to distinguish between Rayleigh or steady state models, and we contend that reality is between these two situations.

In addition to diatom productivity, the process of reverse weathering in sediments is significant in the ARE (Michalopoulos and Aller, 1995, 2004; Rahman et al., 2016), during which the formation of authigenic aluminosilicate from the dissolving bSi, preferentially removes lighter Si isotopes from the pore-water resulting in heavy $\delta^{30}Si_{Si(OH)4}$ signatures of up to 2.0‰ (Tatzel et al., 2015; Ehlert et al., 2016). This process and associated fractionation effect, however, primarily occurs in the sediments. Aller et al. (1996) and DeMaster and Pope (1996) showed that for most Amazon shelf sediments, the diffusive Si flux out of the seabed is minimal, implying that the heavy pore-water signatures are generally not released to the bottom waters in significant amounts. Hydrographic evidences collected during cruise M147 suggest that the surface waters were highly stratified and vertical mixing was very weak. It is thus unlikely that pore-water $\delta^{30}Si_{Si(OH)4}$ would affect the Si isotopic compositions of the surface waters (Chou and Wollast, 2006). As a consequence, the observed non-conservative behavior of both $Si(OH)_4$ and $\delta^{30}Si_{Si(OH)4}$ most likely reflects preferential utilization of lighter Si isotopes during diatom growth in the outer parts of the Amazon River plume. Note that dissolution of fluvial ASi might add $Si(OH)_4$ with light $\delta^{30}Si_{Si(OH)4}$ into the surface water (Frings et al., 2016), which might lower the apparent $Si(OH)_4$ removal and Si isotope fractionation during diatom growth.

Field data collected in February 2012 also reveal significant removal of $Si(OH)_4$ corresponding to elevated $\delta^{30}Si_{Si(OH)4}$ at mid- and high salinities of 15.5-29.1 in the ARE,

401 independent of the selected river water endmembers (Text A2 and Fig. A4a, b). The average
402 isotopic enrichment factor $^{30}\varepsilon$ is estimated to be −1.0±0.4‰ following the Rayleigh model or
403 −1.4±0.5‰ following the steady state model. Both values are consistent with those obtained in
404 May 2018, suggesting that the seasonal variability of Si isotope fractionation during diatom growth
405 is small in the ARE.

406 *4.2.2. Yangtze River Estuary: seasonal variability due to changing hydrological conditions*

407 Both surface $Si(OH)_4$ concentration and isotope distributions fit the two-endmember mixing
408 very well in the YRE (Fig. 3c, d) supporting its conservative behavior during the sampling period
409 in late winter. Measured DIN and DIP concentrations were apparently higher than those predicted
410 from conservative mixing (Fig. 4c, d). We contend that these deviations most likely result from the
411 uncertainty of the river water DIN and DIP endmembers. The close correlations between DIN
412 (R^2=0.98) and DIP (R^2=0.97) and salinity over the entire salinity range essentially suggest
413 exclusive mixing control (Fig. 4c, d). Unlike the ARE, biological effects on Si dynamics are thus
414 negligible, which is supported by the observed low Chl-a concentrations in the YRE (Fig. 2i).

415 Zhang et al. (2015) reported $\delta^{30}Si_{Si(OH)4}$ distributions in the YRE for two other seasons (Fig.
416 5a-d): the dry season of March 2012 with a monthly discharge of 7.0×10^{10} m^3 and the wet season
417 of July 2011 with a monthly discharge of 1.3×10^{11} m^3 (data from Datong observation station;
418 http://www.mwr.gov.cn). These data are included here to assess the seasonal Si dynamics in the
419 YRE. It is noteworthy that Zhang et al. (2015) depicted the same conservative behavior of Si
420 isotopes in the same dry season of March 2012 (Fig. 5a, b). Despite a comparable $Si(OH)_4$
421 concentration range of 5-110 μmol L^{-1} between the two sampling campaigns, $\delta^{30}Si_{Si(OH)4}$ values in
422 this study (1.7-2.6‰) are overall higher than those of 1.5-2.0‰ in Zhang et al. (2015), which is
423 ascribed to a heavier seawater endmember in the former. This large difference between the

seawater endmember values (2.6 vs. 1.7‰) might be a consequence of stronger Si isotope fractionation prevailing during our sampling period, or it likely simply reflects the high temporal and spatial variations in the dynamic shelf system of the East China Sea. In the wet season of July 2011, the river water endmember had $Si(OH)_4$ concentrations and $\delta^{30}Si_{Si(OH)4}$ signatures similar to those in March 2012, while the $\delta^{30}Si_{Si(OH)4}$ of 2.1‰ for the seawater endmember was heavier, even at lower salinities (Fig. 5c, d; Zhang et al., 2015). More importantly, elevated $\delta^{30}Si_{Si(OH)4}$ signatures corresponding to decreased $Si(OH)_4$ beyond the mixing control were observed at high salinities of 24.5 to 30.0 (Fig. 5c, d), which suggests significant Si isotope fractionation during diatom growth in the wet season.

The absence of significant $Si(OH)_4$ utilization at high salinities in late winter before the beginning of spring diatom bloom may be attributed to water temperatures lower than those at which most diatoms can survive in the YRE (Zhang et al., 2015). Moreover, Zhai et al. (2017) addressed the key role of water residence time in constraining biogeochemical processes in the YRE, which would influence the nutrient retention time for developing phytoplankton growth and $Si(OH)_4$ utilization in estuaries (Kemp et al., 2005). Therefore, the residence time of surface waters in the optimal-growth zone (low turbidity and high nutrients) at high salinities needs to be taken into account, which largely depends on the direction and intensity of the trade winds (Lentz, 1995). If the prevailing winds have a component opposite to the flow direction of the river plume, the waters will reside longer in the optimal-growth zone favoring phytoplankton growth (DeMaster et al., 1996). During the sampling periods of this study and Zhang et al. (2015), southeasterly wind prevailed over the shelf neighboring the YRE in July 2011 and weaker northeasterly wind prevailed in March 2012 and 2015 (Fig. 6). The southeasterly wind in summer is generally in the opposite direction of the Yangtze River flow (towards the southeast), which shifts towards the northeast

outside of the YRE mouth. In contrast, the northeasterly wind in winter is overall in the same direction of the plume flow enhancing its offshore transport. In this context, the longer retention time of nutrients favors diatom growth during the summer in the YRE, suggesting that the changing water residence time to some extent contributes to the different seasonal behavior of Si. Unfortunately, data of the residence time of the Yangtze River plume were not collected in both this study and Zhang et al. (2015), which warrants further investigation.

4.2.3. Pearl River Estuary: dominant control by mixing during the sampling period

Surface water $Si(OH)_4$ concentrations at low salinities between 0.0 and 1.6, as well as DIN and DIP, varied within a relatively large range (Figs. 3e and 4e, f), likely suggesting local controls on the variability in the complex upper PRE. However, the corresponding $\delta^{30}Si_{Si(OH)4}$ signatures were essentially constant (Fig. 3f). We thus take the average of these values as the river water endmember for each parameter. Beyond the TMZ at a salinity of 6.5 (Fig. 2m), $Si(OH)_4$, DIN, and DIP concentrations generally decreased along the two-endmember mixing curve suggesting overall conservative behavior, despite DIP concentrations showing relatively large deviations probably resulting from the uncertainty of river water endmember values (Figs. 3e and 4e, f). Within analytical error, $\delta^{30}Si_{Si(OH)4}$ values agree with corresponding mixing predictions (Fig. 3f). The overall conservative distributions of both nutrients and Si isotopes likely point to low phytoplankton growth during estuarine mixing, even in the offshore areas outside of the mouth of the PRE, where both nutrients and light were available in sufficient amounts.

Note that relatively high Chl-a concentrations (>4 $\mu g\ L^{-1}$) were observed at mid-salinities of 16.5 and 24.0 (Fig. 2n) suggesting increased phytoplankton growth, which was, however, insufficient to induce observable removal of any nutrients. One possible reason for the apparently minimal biological utilization of $Si(OH)_4$ is the short residence time of surface waters in the PRE

due to high river discharge and fast flow, which is indicated by the still low salinity of 31.1 for the selected seawater endmember at the outermost station (Fig. 2j). This not only limited the diatom growth but also diminished the signal of potential nutrient removal. Subtle changes of $Si(OH)_4$ and $\delta^{30}Si_{Si(OH)4}$ induced by diatom utilization in the large $Si(OH)_4$ pool may have been masked by strong physical mixing. Lu and Gan (2015) also pointed out that the water residence time plays an important role for the development of phytoplankton blooms during summer in the PRE.

4.3. Differences in Si isotope behavior during estuarine mixing: passage versus reactor

Estuaries can either act as passages of terrestrial Si from the continents to the oceans characterized by conservative behavior of Si or as biogeochemical reactors inducing non-conservative behavior during estuarine mixing and potentially modifying their riverine input fluxes and isotope compositions (Officer, 1979; Zhai et al., 2017). This is supported by the contrasting Si isotope distributions in the large estuaries investigated in this study (i.e., the YRE and PRE acting mainly as passages and the ARE acting mainly as a reactor), as well as significant seasonal variations of $\delta^{30}Si_{Si(OH)4}$ in the YRE (i.e., a passage in winter and a reactor in summer; Zhang et al., 2015), which need to be taken into account for a comprehensive understanding of estuarine Si dynamics and ultimately also the oceanic Si cycle.

Changing diatom productivity in different seasons seems to mainly determine whether an estuary is a passage or a reactor for riverine Si input. However, the mechanisms controlling diatom productivity differ between estuarine systems and climate zones. Besides water residence time, water temperature and light availability also limit diatom growth in the YRE located in the temperate climate zone, in which the primary production rates vary seasonally by nearly two orders of magnitude (Ning et al., 1988). Similarly, surface waters of the Elbe River Estuary also showed a notable increase of $\delta^{30}Si_{Si(OH)4}$ during diatom growth in October relative to in December,

493 indicating a biologically-controlled seasonal variability of Si dynamics in this temperate estuary
494 (Weiss et al., 2015). The PRE, located in the subtropical climate zone, is characterized by dynamic
495 hydrology and biogeochemical processes primarily due to the seasonal variability of the Asian
496 monsoon, river discharge, tidal forcing, and even anthropogenic interferences (Cai et al., 2004).
497 This implies that the PRE varies between passage and reactor of Si as reflected by its seasonally
498 variable and spatially confined diatom blooms (Lu and Gan, 2015).

499 In contrast, the tropical setting and huge size of the Amazon drainage basin minimize changes
500 in freshwater discharge, water temperature, and light availability both within and between years
501 (Nittrouer and DeMaster, 1996). Correspondingly, previous studies only observed small seasonal
502 variations of bSi standing stock, Chl-a concentrations, and the average primary production rate in
503 the optimal-growth zone during an annual cycle (DeMaster et al., 1996), suggesting that the ARE
504 acts as a "continuous reactor", in which diatom growth throughout the year induces strong
505 fractionation of Si isotopes. Our field data collected during two cruises in different seasons
506 showing consistent Si isotope fractionation also support this argument (Text A2). However, not all
507 tropical estuaries display the same pattern. For example, the Indian tropical estuaries show
508 different monsoonal regimes and significant diatom uptake was only identified during winter (i.e.,
509 dry period, northeast monsoon season; Mangalaa et al., 2017). In the tropical Tana River Estuary,
510 $\delta^{30}Si_{Si(OH)4}$ remained stable along the salinity gradient because of the almost complete absence of
511 processes fractionating Si isotopes (Hughes et al., 2012).

512 Estuaries acting as a reactor can efficiently filter and remove riverine Si before it reaches the
513 ocean. This retention is expected to be greater than that of other nutrients because Si is recycled
514 through dissolution of diatom frustules, which is a slow process relative to bacterial
515 remineralization of N and P (Chou and Wollast, 2006). Pioneering work showed that nearly 50%

of the riverine $Si(OH)_4$ flux is removed due to extensive diatom growth in the ARE mixing zone (Milliman and Boyle, 1975) and that 20-40% of the riverine $Si(OH)_4$ flux is buried as bSi in the sediments (Edmond et al., 1981; Shiller, 1996). This is, however, inconsistent with the low bSi content in the Amazon shelf sediments (0.2-0.4 wt% bSi) estimated by DeMaster et al. (1983), which suggested that burial of bSi can account for only a few percent of the riverine $Si(OH)_4$ flux. Consequently, the efficiency of Si retention in high-productivity estuaries was questioned by DeMaster (2002), who argued that a substantial flux of bSi would be exported from the shelf by lateral advection and to a great extent re-dissolve in open ocean waters. Later on, studies (e.g., Michalopoulos and Aller, 2004) pointed out that a large amount of Si may be trapped in deltaic sediments as rapidly formed authigenic clays, little of which would dissolve using the classical bSi-leaching method by DeMaster (1981). Awareness of the substantial underestimation of the quantity of early diagenetic alteration products of bSi was thus raised, in particular in the large tropical estuaries such as the Amazon delta (Michalopoulos and Aller, 2004; Presti and Michalopoulos, 2008). By modifying the bSi-leaching procedure and applying diagenetic models, Michalopoulos and Aller (2004) estimated a bSi burial of ~22% of the riverine $Si(OH)_4$ flux in the ARE. Recently, Rahman et al. (2016, 2017) used cosmogenic ^{32}Si at natural activity levels to determine biologically-produced bSi trapped in rapidly formed authigenic clays and suggested that ~50% of the riverine $Si(OH)_4$ flux may be buried in the Amazon delta.

In this study, $Si(OH)_4$ removal in the ARE is estimated to be 47-55% at mid- and high salinities of 15.5-29.1 in February 2012 (Text A2) and 44±7% at mid-salinities of 6.7-27.3 in May 2018 based on the two-endmember mixing model (Text A3). We thus follow the latest study (i.e., Rahman et al., 2016, 2017) and take 50% as the filtering capacity of $Si(OH)_4$ in the ARE. Combined with the isotopic enrichment factor $^{30}\varepsilon$ of −1.0±0.4‰ or −1.6±0.4‰ obtained in the ARE, the

539 $\delta^{30}Si_{Si(OH)4}$ signatures entering the Atlantic Ocean from the ARE increase by 0.7±0.2‰ following
540 the Rayleigh model (Eq. 1) or 0.8±0.2‰ following the steady state model (Eq. 4). Note that a part
541 of bSi formed during $Si(OH)_4$ removal might be exported and re-dissolve in the open ocean, which
542 would release light Si isotope signatures into the surrounding water. In this context, the estimated
543 increase of 0.7-0.8‰ is most likely an upper limit.

544 **4.4. Implications for the Si isotopic composition of the global riverine input to the ocean**

545 Globally, Frings et al. (2016) adopted a low filtering capacity of 10% based on earlier work
546 of DeMaster (2002) and estimated an increase of ~0.1‰ in riverine $\delta^{30}Si_{Si(OH)4}$ signatures entering
547 the ocean. However, Treguer and De La Rocha (2013) re-estimated the estuarine removal flux of
548 Si to be 1.5±0.5 Tmol yr^{-1} consisting of bSi deposition and its storage via authigenic clay
549 formations, which is consistent with the preservation flux in proximal coastal zones (~1.4 Tmol
550 yr^{-1}) estimated by Laruelle et al. (2009). We thus adopt the global estuarine filtering capacity of
551 ~22% in Treguer and De La Rocha (2013). Assuming that all the estuarine Si removal induces Si
552 isotope fractionation and applying the isotopic enrichment factor $^{30}\varepsilon$ of −1.0±0.4‰ or −1.6±0.4‰
553 obtained in the ARE, the increase of riverine $\delta^{30}Si_{Si(OH)4}$ signatures entering the ocean globally is
554 estimated to be 0.2±0.1‰ (Rayleigh model; Eq. 1) or 0.3±0.2‰ (steady state model; Eq. 4). We
555 contend that this is a first order estimation, which needs further constraints, while several on-going
556 studies suggest that the global estuarine Si removal flux of 1.5±0.5 Tmol yr^{-1} is likely an
557 underestimation. For example, Rahman et al. (2017) revisited Si sink in different delta systems
558 and pointed out a higher sedimentary Si storage flux of 3.5-3.9 Tmol yr^{-1} as authigenic clay in
559 tropical and subtropical deltas. In this context, our estimation of 0.2-0.3‰ probably represents a
560 lower limit of the increase in $\delta^{30}Si_{Si(OH)4}$ by global estuaries. This also suggests that the estuarine
561 reactors potentially exert a much larger influence on riverine Si isotope fluxes than previously

thought.

5. CONCLUSIONS

$\delta^{30}Si_{Si(OH)4}$ in the ARE, YRE, and PRE displayed significant differences in distribution patterns, reflecting the role of large river estuaries as either a passage or a reactor in delivering riverine Si to the ocean. While conservative mixing between river water and seawater primarily modulated both surface $Si(OH)_4$ concentrations and $\delta^{30}Si_{Si(OH)4}$ signatures in the YRE and PRE presented in this study, significant Si isotope fractionation during diatom growth was observed over the entire salinity range in the ARE. We estimate isotopic enrichment factors $^{30}\varepsilon$ of −1.0±0.4‰ (Rayleigh model) or −1.6±0.4‰ (steady state model) in the ARE, both of which are within error consistent with the consensus average value of −1.1‰ in various oceanic settings. Applying these $^{30}\varepsilon$ values, we re-evaluate the influence that estuaries exert on the land-to-ocean Si isotope fluxes on a global scale and suggest that the present riverine $\delta^{30}Si_{Si(OH)4}$ input signature into the ocean is elevated by 0.2-0.3‰ compared to scenarios without estuarine diatom productivity. In addition, distinct seasonal variations of Si isotope behavior in the YRE are found by comparing our data to previously reported measurements. This seasonality and its underlying causes require future examination in large river estuaries for comprehensively understanding their impacts on the global Si cycle and the Si isotope mass balance.

ACKNOWLEDGEMENTS

This work was funded by the National Key Scientific Research Project (2015CB954003) sponsored by the Ministry of Science and Technology of China and by the National Natural Science Foundation of China (NSFC) through grant 41606089. Zhouling Zhang was co-supported by a scholarship under the Graduate School of Xiamen University and the National Key Scientific Research Project (2015CB954001). Henning Kuhnert was supported by the DFG Research Center "The Ocean in the Earth System". Cristiano M. Chiessi acknowledges the financial support from FAPESP (2012/17517-3). We thank the R/V *Meteor* cruise M147 crew and the R/V *Maria S. Merian* cruise MSM20/3 crew for technical support during sampling in the ARE. Data acquisition and sample collection in the YRE were conducted onboard R/V *Runjiang I* supported by a Shiptime Sharing Project of the NSFC (NORC2015-03). We thank Guipeng Yang for providing the Chl-a data and Zhiqiang Liu for providing the wind data in the YRE. We thank Kerstin Nachtigall, Andre Mutzberg, Lifang Wang, Biyan He, Wei Qian, Weidong Zhai, Pengfei Liu, and Gila Merschel for their assistance in sampling and/or analysis. We also thank Paul Treguer, Christina De La Rocha, and Shaily Rahman for providing helpful discussion. We would like to thank Damien Cardinal, Gregory de Souza, and two anonymous reviewer for their constructive comments on the manuscript.

REFERENCES

Aller R.C., Blair N.E., Xia Q. and Rude P.D. (1996) Remineralization rates, recycling, and storage of carbon in Amazon shelf sediments. *Cont. Shelf Res.* **16**, 753-786.

Anderson G.F. (1986) Silica, Diatoms and a Freshwater Productivity Maximum in Atlantic Coastal Plain Estuaries, Chesapeake Bay. *Estuar. Coast. Shelf Sci.* **22**, 183-197.

Beucher C.P., Brzezinski M.A. and Jones J.L. (2008) Sources and biological fractionation of Silicon isotopes in the Eastern Equatorial Pacific. *Geochim. Cosmochim. Acta* **72**, 3063-3073.

Beusen A.H.W., Bouwman A.F., Durr H.H., Dekkers A.L.M. and Hartmann J. (2009) Global patterns of dissolved silica export to the coastal zone: Results from a spatially explicit global model. *Global Biogeochem. Cycles* **23**, GB0A02.

Cai W.-J., Dai M., Wang Y., Zhai W., Huang T., Chen S., Zhang F., Chen Z. and Wang Z. (2004) The biogeochemistry of inorganic carbon and nutrients in the Pearl River estuary and the adjacent Northern South China Sea. *Cont. Shelf Res.* **24**, 1301-1319.

Cao Z., Frank M. and Dai M. (2015) Dissolved silicon isotopic compositions in the East China Sea: Water mass mixing vs. biological fractionation. *Limnol. Oceanogr.* **60**, 1619-1633.

Cao Z., Frank M., Dai M., Grasse P. and Ehlert C. (2012) Silicon isotope constraints on sources and utilization of silicic acid in the northern South China Sea. *Geochim. Cosmochim. Acta* **97**, 88-104.

Carbonnel V., Vanderborght J.-P., Lionard M. and Chou L. (2013) Diatoms, silicic acid and biogenic silica dynamics along the salinity gradient of the Scheldt estuary (Belgium/The Netherlands). *Biogeochemistry* **113**, 657-682.

Chou L. and Wollast R. (2006) Estuarine silicon dynamics. In *The Silicon Cycle: Human*

Perturbations and Impacts on Aquatic Systems (eds. D. Ittekkot, C. Unger, C. Humborg and N. Tac An). Scientific Committee on Problems of the Environment.

Conley D.J. (2002) Terrestrial ecosystems and the global biogeochemical silica cycle. *Global Biogeochem. Cycles* **16**, 1121.

Conley D.J. and Malone T.C. (1992) Annual Cycle of Dissolved Silicate in Chesapeake Bay - Implications for the Production and Fate of Phytoplankton Biomass. *Mar. Ecol. Prog. Ser.* **81**, 121-128.

Conley D.J., Likens G.E., Buso D.C., Saccone L., Bailey S.W. and Johnson C.E. (2008) Deforestation causes increased dissolved silicate losses in the Hubbard Brook Experimental Forest. *Glob. Change Biol.* **14**, 2548–2554.

Davidson E.A., de Araujo A.C., Artaxo P., Balch J.K., Brown I.F., MM C.B., Coe M.T., DeFries R.S., Keller M., Longo M., Munger J.W., Schroeder W., Soares-Filho B.S., Souza C.M., Jr. and Wofsy S.C. (2012) The Amazon basin in transition. *Nature* **481**, 321-328.

De La Rocha C.L., Brzezinski M.A. and DeNiro M.J. (1997) Fractionation of silicon isotopes by marine diatoms during biogenic silica formation. *Geochim. Cosmochim. Acta* **61**, 5051-5056.

Delvaux C., Cardinal D., Carbonnel V., Chou L., Hughes H.J. and André L. (2013) Controls on riverine $\delta^{30}Si$ signatures in a temperate watershed under high anthropogenic pressure (Scheldt - Belgium). *J. Mar. Sys.* **128**, 40-51.

DeMaster D.J. (1981) The Supply and Accumulation of Silica in the Marine Environment. *Geochim. Cosmochim. Acta* **45**, 1715-1732.

DeMaster D.J. (2002) The accumulation and cycling of biogenic silica in the Southern Ocean: revisiting the marine silica budget. *Deep-Sea Res. Pt II* **49**, 3155-3167.

642 DeMaster D.J., Knapp G.B. and Nittrouer C.A. (1983) Biological Uptake and Accumulation of
643 Silica on the Amazon Continental-Shelf. *Geochim. Cosmochim. Acta* **47**, 1713-1723.
644 DeMaster D.J. and Pope R.H. (1996) Nutrient dynamics in Amazon shelf waters: Results from
645 AMASSEDS. *Cont. Shelf Res.* **16**, 263-289.
646 DeMaster D.J., Smith W.O., Nelson D.M. and Aller J.Y. (1996) Biogeochemical processes in
647 Amazon shelf waters: Chemical distributions and uptake rates of silicon, carbon and
648 nitrogen. *Cont. Shelf Res.* **16**, 617-643.
649 Ding T.P., Gao J.F., Tian S.H., Shi G.Y., Chen F., Wang C.Y., Luo X.R. and Han D. (2014)
650 Chemical and Isotopic Characteristics of the Water and Suspended Particulate Materials in
651 the Yangtze River and Their Geological and Environmental Implications. *Acta Geologica*
652 *Sinica-English Edition* **88**, 276-360.
653 Du C., Liu Z., Dai M., Kao S.J., Cao Z., Zhang Y., Huang T., Wang L. and Li Y. (2013) Impact of
654 the Kuroshio intrusion on the nutrient inventory in the upper northern South China Sea:
655 insights from an isopycnal mixing model. *Biogeosciences* **10**, 6419-6432.
656 Edmond J.M., Boyle E.A., Grant B. and Stallard R.F. (1981) The Chemical Mass Balance in the
657 Amazon Plume I - the Nutrients. *Deep-Sea Res.* **28**, 1339-1374.
658 Edmond J.M., Spivack A., Grant B.C., Hu M.H., Chen Z.X., Chen S. and Zeng X.S. (1985)
659 Chemical-Dynamics of the Changjiang Estuary. *Cont. Shelf Res.* **4**, 17-36.
660 Ehlert C., Doering K., Wallmann K., Scholz F., Sommer S., Grasse P., Geilert S. and Frank M.
661 (2016) Stable silicon isotope signatures of marine pore waters – Biogenic opal dissolution
662 versus authigenic clay mineral formation. *Geochim. Cosmochim. Acta* **191**, 102-117.
663 Frings P.J., Clymans W., Fontorbe G., De La Rocha C.L. and Conley D.J. (2016) The continental
664 Si cycle and its impact on the ocean Si isotope budget. *Chem. Geol.* **425**, 12-36.

665 Fripiat, F., Cavagna A.-J., Savoye N., Dehairs F., André L. and Cardinal D. (2011) Isotopic
666 constraints on the Si-biogeochemical cycle of the Antarctic Zone in the Kerguelen area
667 (KEOPS). *Mar. Chem.* **123**, 11-22.
668 Gao L., Li D. and Zhang Y. (2012) Nutrients and particulate organic matter discharged by the
669 Changjiang (Yangtze River): Seasonal variations and temporal trends. *J. Geophys. Res.*
670 *Biogeosci.* **117**, G04001.
671 Georg R.B., Reynolds B.C., Frank M. and Halliday A.N. (2006) New sample preparation
672 techniques for the determination of Si isotopic compositions using MC-ICPMS. *Chem.*
673 *Geol.* **235**, 95-104.
674 Grasse P., Brzezinski M.A., Cardinal D., de Souza G.F., Andersson P., Closset I., Cao Z., Dai M.,
675 Ehlert C., Estrade N., François R., Frank M., Jiang G., Jones J.L., Kooijman E., Liu Q., Lu
676 D., Pahnke K., Ponzevera E., Schmitt M., Sun X., Sutton J.N., Thil F., Weis D., Wetzel F.,
677 Zhang A., Zhang J. and Zhang Z. (2017) GEOTRACES inter-calibration of the stable
678 silicon isotope composition of dissolved silicic acid in seawater. *J. Anal. At. Spectrom.* **32**,
679 562-578.
680 Harrison P.J., Yin K., Lee J.H.W., Gan J. and Liu H. (2008) Physical–biological coupling in the
681 Pearl River Estuary. *Cont. Shelf Res.* **28**, 1405-1415.
682 He B., Dai M., Zhai W., Guo X. and Wang L. (2014) Hypoxia in the upper reaches of the Pearl
683 River Estuary and its maintenance mechanisms: A synthesis based on multiple year
684 observations during 2000–2008. *Mar. Chem.* **167**, 13-24.
685 Hughes H.J., Delvigne C., Korntheuer M., de Jong J., André L. and Cardinal D. (2011) Controlling
686 the mass bias introduced by anionic and organic matrices in silicon isotopic measurements
687 by MC-ICP-MS. *J. Anal. At. Spectrom.* **26**, 1892-1896.

688 Hughes H.J., Bouillon S., André L. and Cardinal D. (2012) The effects of weathering variability
689 and anthropogenic pressures upon silicon cycling in an intertropical watershed (Tana River,
690 Kenya). *Chem. Geol.* **308-309**, 18-25.
691 Hydes D.J., Aoyama M., Aminot A., Bakker K., Becker S., Coverly S., Daniel A., Dickson A.G.,
692 Grosso O., Kerouel R., van Ooijen J., Sato K., Tanhua T., Woodward E.M.S. and Zhang
693 J.Z. (2010) Recommendations for the determination of nutrients in seawater to high levels
694 of precision and inter-comparability using continuous flow analysers. *The GO-SHIP*
695 *Repeat Hydrography Manual: A Collection of Expert Reports and Guidelines* (eds. E.M.
696 Hood, C.L. Sabine and B.M. Sloyan). IOCCP Report Number 14, ICPO Publication Series
697 Number 134.
698 Johns W.E., Lee T.N., Beardsley R.C., Candela J., Limeburner R. and Castro B. (1998) Annual
699 cycle and variability of the North Brazil Current. *J. Phys. Oceanogr* **28**, 103-128.
700 Jones M.T., Pearce C.R. and Oelkers E.H. (2012) An experimental study of the interaction of
701 basaltic riverine particulate material and seawater. *Geochim. Cosmochim. Acta* **77**, 108-
702 120.
703 Kemp W.M., Boynton W.R., Adolf J.E., Boesch D.F., Boicourt W.C., Brush G., Cornwell J.C.,
704 Fisher T.R., Glibert P.M., Hagy J.D., Harding L.W., Houde E.D., Kimmel D.G., Miller
705 W.D., Newell R.I.E., Roman M.R., Smith E.M. and Stevenson J.C. (2005) Eutrophication
706 of Chesapeake Bay: historical trends and ecological interactions. *Mar. Ecol. Prog. Ser.* **303**,
707 1-29.
708 Laruelle G.G., Roubeix V., Sferratore A., Brodherr B., Ciuffa D., Conley D.J., Dürr H.H., Garnier
709 J., Lancelot C., Le Thi Phuong Q., Meunier J.D., Meybeck M., Michalopoulos P., Moriceau
710 B., Ní Longphuirt S., Loucaides S., Papush L., Presti M., Ragueneau O., Regnier P.,

711 Saccone L., Slomp C.P., Spiteri C. and Van Cappellen P. (2009) Anthropogenic
712 perturbations of the silicon cycle at the global scale: Key role of the land-ocean transition.
713 *Global Biogeochem. Cycles* **23**, GB4031.
714 Latrubesse E.M., Arima E.Y., Dunne T., Park E., Baker V.R., d'Horta F.M., Wight C., Wittmann F.,
715 Zuanon J., Baker P.A., Ribas C.C., Norgaard R.B., Filizola N., Ansar A., Flyvbjerg B. and
716 Stevaux J.C. (2017) Damming the rivers of the Amazon basin. *Nature* **546**, 363-369.
717 Lehtimäki M., Tallberg P. and Siipola V. (2013) Seasonal Dynamics of Amorphous Silica in Vantaa
718 River Estuary. *Silicon* **5**, 35-51.
719 Lentz S.J. (1995) The Amazon River Plume during AMASSEDS: Subtidal current variability and
720 the importance of wind forcing. *J. Geophys. Res.* **100**, 2377-2390.
721 Li M., Xu K., Watanabe M. and Chen Z. (2007) Long-term variations in dissolved silicate, nitrogen,
722 and phosphorus flux from the Yangtze River into the East China Sea and impacts on
723 estuarine ecosystem. *Estuar. Coast. Shelf Sci.* **71**, 3-12.
724 Liu S.M., Hong G.H., Zhang J., Ye X.W. and Jiang X.L. (2009) Nutrient budgets for large Chinese
725 estuaries. *Biogeosciences* **6**, 2245-2263.
726 Lu Z. and Gan J. (2015) Controls of seasonal variability of phytoplankton blooms in the Pearl
727 River Estuary. *Deep Sea Res. Part II* **117**, 86-96.
728 Mangalaa K.R., Cardinal D., Brajard J., Rao D.B., Sarma N.S., Djouraev I., Chiranjeevulu G.,
729 Murty K.N. and Sarma V.V.S.S. (2017) Silicon cycle in Indian estuaries and its control by
730 biogeochemical and anthropogenic processes. *Cont. Shelf Res.* **148**, 64-88.
731 Meade R.H., Dunne T., Richey J.E., U D.M.S. and Salati E. (1985) Storage and remobilization of
732 suspended sediment in the lower Amazon river of Brazil. *Science* **228**, 488-490.
733 Meyerink S., Ellwood M.J., Maher W.A. and Strzepek R. (2017) Iron availability influences silicon

isotope fractionation in two Southern Ocean diatoms (*Proboscia inermis* and *Eucampia antarctica*) and a coastal diatom (*Thalassiosira pseudonana*). *Front. Mar. Sci.* **4**, 217.

Meyerink S.W., Boyd P.W., Maher W.A., Milne A., Strzepek R. and Ellwood M.J. (2019) Putting the silicon cycle in a bag: Field and mesocosm observations of silicon isotope fractionation in subtropical waters east of New Zealand. *Mar. Chem.* **213,** 1-12.

Michalopoulos P. and Aller R. C. (1995) Rapid clay mineral formation in Amazon delta sediments: Reverse weathering and oceanic emental cycles. *Science* **270**, 614–617.

Michalopoulos P. and Aller R.C. (2004) Early diagenesis of biogenic silica in the Amazon delta: alteration, authigenic clay formation, and storage. *Geochim. Cosmochim. Acta* **68**, 1061-1085.

Milliman J.D. and Boyle E. (1975) Biological uptake of dissolved silica in the Amazon river estuary. *Science* **189**, 995-997.

Milligan A.J., Varela D.E., Brzezinski M.A. and Morel F.M.M. (2004) Dynamics of silicon metabolism and silicon isotopic discrimination in a marine diatom as a function of pCO_2. *Limnol. Oceanogr.* **49**, 322-329.

Moquet J.S., Guyot J.L., Crave A., Viers J., Filizola N., Martinez J.M., Oliveira T.C., Sanchez L.S., Lagane C., Casimiro W.S., Noriega L. and Pombosa R. (2016) Amazon River dissolved load: temporal dynamics and annual budget from the Andes to the ocean. *Environ. Sci. Pollut. Res. Int.* **23**, 11405-11429.

Nelson D.M. and Dortch Q. (1996) Silicic acid depletion and silicon limitation in the plume of the Mississippi River: Evidence from kinetic studies in spring and summer. *Mar. Ecol. Prog. Ser.* **136**, 163-178.

Ning X.R., Vaulot D., Liu Z.S. and Liu Z.L. (1988) Standing Stock and Production of

Phytoplankton in the Estuary of the Changjiang (Yangtse River) and the Adjacent East China Sea. *Mar. Ecol. Prog. Ser.* **49**, 141-150.

Nittrouer C.A. and DeMaster D.J. (1996) The Amazon shelf setting: Tropical, energetic, and influenced by a large river. *Cont. Shelf Res.* **16**, 553-573.

Nguyen T.T.N., Némery J., Gratiot N., Garnier J., Strady E., Tran V.Q., Nguyen A.T., Nguyen T.N.T., Golliet C. and Aimé J. (2019) Phosphorus adsorption/desorption processes in the tropical Saigon River estuary (Southern Vietnam) impacted by a megacity. *Estuar. Coast. Shelf Sci.* **227**, 106321.

Oelkers E.H., Gislason S.R., Eiriksdottir E.S., Jones M., Pearce C.R. and Jeandel C. (2011) The role of riverine particulate material on the global cycles of the elements. *Appl. Geochem.* **26**, S365-S369.

Officer C.B. (1979) Discussion of the behavior of nonconservative dissolved constituents in estuaries. *Estuar. Coast. Mar. Sci.* **9**, 91-94.

Pastuszak M., Conley D.J., Humborg C., Witek Z. and Sitek S. (2008) Silicon dynamics in the Oder estuary, Baltic Sea. *J. Mar. Sys.* **73**, 250-262.

Patra S., Liu C.Q., Wang F.S., Li S.L. and Wang B.L. (2012) Behavior of major and minor elements in a temperate river estuary to the coastal sea. *Int. J. Environ. Sci. Technol.* **9**, 647-654.

Presti M. and Michalopoulos P. (2008) Estimating the contribution of the authigenic mineral component to the long-term reactive silica accumulation on the western shelf of the Mississippi River Delta. *Cont. Shelf Res.* **28**, 823-838.

Rahman S., Aller R.C. and Cochran J.K. (2016) Cosmogenic ^{32}Si as a tracer of biogenic silica burial and diagenesis: Major deltaic sinks in the silica cycle. *Geophys. Res. Lett.* **43**, 7124-7132.

780 Rahman S., Aller R.C. and Cochran J.K. (2017) The Missing Silica Sink: Revisiting the Marine
781 Sedimentary Si Cycle Using Cosmogenic ^{32}Si. *Global Biogeochem. Cycles* **31**, 1559-1578.
782 Reynolds B., Frank M. and Halliday A. (2006) Silicon isotope fractionation during nutrient
783 utilization in the North Pacific. *Earth. Planet. Sci. Lett.* **244**, 431-443.
784 Reynolds B.C., Aggarwal J., André L., Baxter D., Beucher C., Brzezinski M.A., Engström E.,
785 Georg R.B., Land M., Leng M.J., Opfergelt S., Rodushkin I., Sloane H.J., van den Boorn
786 S.H.J.M., Vroon P.Z. and Cardinal D. (2007) An inter-laboratory comparison of Si isotope
787 reference materials. *J. Anal. At. Spectrom.* **22**, 561-568.
788 Shiller A.M. (1996) Effect of recycling traps and upwelling on estuarine chemical flux estimates.
789 *Geochim. Cosmochim. Acta* **60**, 3177-3185.
790 Singurindy, O., Berkowitz B. and Lowell R.P. (2004) Carbonate dissolution and precipitation in
791 coastal environments: Laboratory analysis and theoretical consideration. Water Resour.
792 Res. **40**, W04401.
793 Smith W.O. and Demaster D.J. (1996) Phytoplankton biomass and productivity in the Amazon
794 River plume: Correlation with seasonal river discharge. *Cont. Shelf Res.* **16**, 291-319.
795 Sutton J.N., André L., Cardinal D., Conley D.J., de Souza G.F., Dean J., Dodd J., Ehlert C.,
796 Ellwood M.J., Frings P.J., Grasse P., Hendry K., Leng M.J., Michalopoulos P., Panizzo V.N.
797 and Swann G.E.A. (2018) A Review of the Stable Isotope Bio-geochemistry of the Global
798 Silicon Cycle and Its Associated Trace Elements. *Front. Earth. Sci.* **5**, 112.
799 Sutton J.N., Varela D.E., Brzezinski M.A. and Beucher C.P. (2013) Species-dependent silicon
800 isotope fractionation by marine diatoms. *Geochim. Cosmochim. Acta* **104**, 300-309.
801 Tatzel M., von Blanckenburg F., Oelze M., Schuessler J.A. and Bohrmann G. (2015) The silicon
802 isotope record of early silica diagenesis. *Earth. Planet. Sci. Lett.* **428**, 293-303.

803 Treguer P.J. and De La Rocha C.L. (2013) The world ocean silica cycle. *Annu. Rev. Mar. Sci.* **5**,
804 477-501.
805 van den Boorn S. H. J. M., Vroon P. Z. and Van Bergen M. J. (2009) Sulfur-induced offsets in MC-
806 ICP-MS silicon-isotope measurements. *J. Anal. At. Spectrom.* **24**, 1111–1114.
807 Van Heukelem L. and Thomas C.S. (2001) Computer-assisted high-performance liquid
808 chromatography method development with applications to the isolation and analysis of
809 phytoplankton pigments. *J. Chromatogr. A* **910**, 31-49.
810 Varela, D.E., Pride C.J. and Brzezinski M.A. (2004) Biological fractionation of silicon isotopes in
811 Southern Ocean surface waters. *Global Biogeochem. Cycles* **18**, GB1047.
812 Wang Y., Shen J., He Q., Zhu L. and Zhang D. (2015) Seasonal variations of transport time of
813 freshwater exchanges between Changjiang Estuary and its adjacent regions. *Estuar. Coast.*
814 *Shelf Sci.* **157**, 109-119.
815 Weiss A., De La Rocha C., Amann T. and Hartmann J. (2015) Silicon isotope composition of
816 dissolved silica in surface waters of the Elbe Estuary and its tidal marshes. *Biogeochemistry*
817 **124**, 61-79.
818 Zhai W.-D., Yan X.-L. and Qi D. (2017) Biogeochemical generation of dissolved inorganic carbon
819 and nitrogen in the North Branch of inner Changjiang Estuary in a dry season. *Estuar.*
820 *Coast. Shelf Sci.* **197**, 136-149.
821 Zhang A.Y., Zhang J., Hu J., Zhang R.F. and Zhang G.S. (2015) Silicon isotopic chemistry in the
822 Changjiang Estuary and coastal regions: Impacts of physical and biogeochemical processes
823 on the transport of riverine dissolved silica. *J. Geophys. Res. Oceans* **120**, 6943-6957.
824 Zhang J., Ren J.L., Liu S.M., Zhang Z.F., Wu Y., Xiong H. and Chen H.T. (2003) Dissolved
825 aluminum and silica in the Changjiang (Yangtze River): Impact of weathering in

826 subcontinental scale. *Global Biogeochem. Cycles* **17**, 1077.
827 Zhang J., Yu Z.G., Wang J.T., Ren J.L., Chen H.T., Xiong H., Dong L.X. and Xu W.Y. (1999) The
828 subtropical Zhujiang (Pearl River) Estuary: Nutrient, trace species and their relationship to
829 photosynthesis. *Estuar. Coast. Shelf Sci.* **49**, 385-400.
830 Zhang, Z., Sun, X., Dai, M., Cao, Z., Fontorbe, G. and Conley, D.J. (2019) Impact of human
831 disturbance on the biogeochemical silicon cycle in a coastal sea revealed by silicon isotopes.
832 *Limnol. Oceanogr.* doi:10.1002/lno.11320.

Table 1. Salinity, dissolved silicate ($Si(OH)_4$) concentrations, and dissolved silicon isotopic compositions ($\delta^{30}Si_{Si(OH)4}$) in the surface waters of the Amazon, Yangtze, and Pearl River estuaries and adjacent shelf areas. "Bracketing measurement" denotes $\delta^{30}Si_{Si(OH)4}$ analysis for a sample on a single day. "Mean" denotes the average $\delta^{30}Si_{Si(OH)4}$ based on repeated bracketing measurements from different days. "Final reported data" present $\delta^{30}Si_{Si(OH)4}$ of the mean except that for two samples measured once, $\delta^{30}Si_{Si(OH)4}$ of bracketing measurement was used.

					Bracketing measurement			**Mean**	**Final reported data**
					I	II	III		
Station	**Lat. (°N)**	**Long. (°E)**	**Salinity**	**$Si(OH)_4$ (μmol L^{-1})**	**$\delta^{30}Si_{Si(OH)4}$ (‰ ± $2SD_{bracketing}$)[§]**	**$\delta^{30}Si_{Si(OH)4}$ (‰ ± $2SD_{bracketing}$)[§]**	**$\delta^{30}Si_{Si(OH)4}$ (‰ ± $2SD_{bracketing}$)[§]**	**$\delta^{30}Si_{Si(OH)4}$ (‰ ± $2SD_{repeated}$)[‡]**	**$\delta^{30}Si_{Si(OH)4}$ (‰ ± 2SD)[†]**
Amazon River Estuary (May 2018)									
M147_66-1*	0.05	−48.71	0.0	150.2	1.29 ± 0.03	1.18 ± 0.21	1.10 ± 0.03	1.19 ± 0.19	1.19 ± 0.20
M147_70-1	0.02	−48.42	0.8	147.2					
M147_69-1	0.02	−48.42	2.3	141.2					
M147_71-1*	0.03	−48.19	4.0	124.5	1.74 ± 0.31	1.60 ± 0.24		1.67 ± 0.20	1.67 ± 0.20
M147_80-1*	1.27	−48.28	6.7	66.0	2.05 ± 0.10	1.91 ± 0.20		1.98 ± 0.20	1.98 ± 0.20
M147-79-1	1.48	−48.15	10.7	67.8					
M147_78-1	1.57	−48.09	13.4	58.3					
M147_72-1	0.57	−48.00		50.6					
M147_75-1*	1.65	−48.04	16.5	43.9	2.04 ± 0.28	1.89 ± 0.20		1.97 ± 0.21	1.97 ± 0.21
M147_74-1	1.74	−47.97	20.4	31.0					
M147_64-1*	1.94	−47.79	27.3	16.3	1.81 ± 0.20	1.70 ± 0.12		1.75 ± 0.15	1.75 ± 0.20
M147_56-F*	2.08	−47.67	30.0	1.3	3.08 ± 0.22	2.96 ± 0.20		3.02 ± 0.17	3.02 ± 0.20

M147_55-F	2.32	−47.47	35.0	0.6					
Yangtze River Estuary (March 2015)									
C4	31.51	121.43	0.2	101.5	1.74 ± 0.15				1.74 ± 0.20
C5	31.41	121.55	0.2	106.3	1.79 ± 0.09	1.78 ± 0.20		1.79 ± 0.01	1.79 ± 0.20
C6	31.35	121.68	0.2	101.5	1.80 ± 0.16	1.77 ± 0.26		1.79 ± 0.04	1.79 ± 0.20
C7	31.24	121.79	0.2	101.5	1.69 ± 0.16	1.71 ± 0.21		1.70 ± 0.03	1.70 ± 0.20
A06-1	31.05	122.06	7.5	87.2	1.93 ± 0.08	1.84 ± 0.18		1.89 ± 0.13	1.89 ± 0.20
A06-2	30.95	122.25	16.0	58.7	2.00 ± 0.19	2.10 ± 0.06		2.05 ± 0.14	2.05 ± 0.20
A06-3	30.90	122.38	21.0	49.2	2.05 ± 0.11	2.03 ± 0.20		2.04 ± 0.03	2.04 ± 0.20
A06-4	30.87	122.50	22.5	41.1	2.04 ± 0.15	2.05 ± 0.13	2.13 ± 0.18	2.07 ± 0.10	2.07 ± 0.20
A06-7*	30.72	123.00	31.2	19.4	1.95 ± 0.15	1.96 ± 0.20		1.96 ± 0.01	1.96 ± 0.20
A06-9*	30.56	123.50	33.6	11.3	2.13 ± 0.14	2.07 ± 0.13		2.10 ± 0.08	2.10 ± 0.20
A06-11*	30.43	123.99	34.0	9.2	2.62 ± 0.11	2.60 ± 0.21		2.61 ± 0.03	2.61 ± 0.20
Pearl River Estuary (August 2012)									
P04	22.99	113.54	0.0	166.6	1.41 ± 0.15	1.47 ± 0.08		1.44 ± 0.08	1.44 ± 0.20
A01	22.74	113.66	1.0	146.5	1.35 ± 0.14				1.35 ± 0.20
A02	22.68	113.70	0.9	147.8	1.44 ± 0.10	1.45 ± 0.13		1.45 ± 0.01	1.45 ± 0.20
A03	22.61	113.71	1.6	128.8	1.38 ± 0.08	1.35 ± 0.12		1.37 ± 0.04	1.37 ± 0.20
A04	22.52	113.75	1.3	129.4	1.32 ± 0.05	1.43 ± 0.14		1.38 ± 0.16	1.38 ± 0.20
A05	22.45	113.76	6.5	120.9	1.39 ± 0.15	1.33 ± 0.24	1.42 ± 0.14	1.38 ± 0.09	1.38 ± 0.20
A06	22.40	113.77	8.1	114.5	1.50 ± 0.14	1.47 ± 0.13		1.49 ± 0.04	1.49 ± 0.20
A07	22.29	113.81	11.8	97.6	1.57 ± 0.21	1.47 ± 0.25		1.52 ± 0.14	1.52 ± 0.20
A08	22.26	113.82	16.5	77.7	1.71 ± 0.03	1.77 ± 0.16		1.74 ± 0.08	1.74 ± 0.20
A10	22.14	113.80	19.1	80.2	1.53 ± 0.13	1.45 ± 0.07		1.49 ± 0.11	1.49 ± 0.20
F406	22.19	113.78	21.2	60.8	1.72 ± 0.07	1.81 ± 0.18		1.77 ± 0.13	1.77 ± 0.20
F412	22.07	113.90	23.5	49.3	1.65 ± 0.13	1.77 ± 0.17	1.60 ± 0.11	1.67 ± 0.17	1.67 ± 0.20
F413	22.03	113.94	25.2	43.9	1.69 ± 0.15	1.71 ± 0.21		1.70 ± 0.03	1.70 ± 0.20

F414*	22.00	113.97	27.7	34.9	1.73 ± 0.08	1.82 ± 0.24	1.78 ± 0.13	1.78 ± 0.20
F415*	21.96	114.01	31.1	14.9	1.76 ± 0.20	1.60 ± 0.15	1.68 ± 0.23	1.68 ± 0.23

838 § ‰ ± $2SD_{bracketing}$ is the average $\delta^{30}Si_{Si(OH)4}$ together with 2 standard deviations estimated from the bracketing measurements on a single

839 day.

840 ‡ ‰ ± $2SD_{repeated}$ is the average $\delta^{30}Si_{Si(OH)4}$ together with 2 standard deviations estimated from the repeated bracketing measurements

841 from different days.

842 † 2SD for the final reported data represents the long-term external reproducibility of ±0.20‰, except that for few samples with $2SD_{repeated}$

843 larger than ±0.20‰, the $2SD_{repeated}$ was used.

844 * $Si(OH)_4$ in the samples was pre-concentrated via brucite coprecipitation before cation-exchange chromatography.

Figure Captions

Figure 1. Bathymetric map showing the locations of sampling stations in the Amazon, Yangtze, and Pearl River estuaries and adjacent shelf areas.

Figure 2. Surface distributions of salinity (a, e, and j), dissolved silicate ($Si(OH)_4$; b, f, and k), dissolved silicon isotopic compositions ($\delta^{30}Si_{Si(OH)4}$; c, g, and l), total suspended matter (TSM; h and m), and chlorophyll a (Chl-a; d, i, and n) in the Amazon (upper), Yangtze (middle), and Pearl (below) River estuaries and adjacent shelf areas.

Figure 3. Dissolved silicate ($Si(OH)_4$) concentrations and dissolved silicon isotopic compositions ($\delta^{30}Si_{Si(OH)4}$) distributions along salinity gradients in the Amazon (a and b), Yangtze (c and d), and Pearl (e and f) River estuaries. The solid lines in each panel predict the conservative mixing for $Si(OH)_4$ or $\delta^{30}Si_{Si(OH)4}$ between the river water and seawater endmembers, which are selected according to field measurements at the lowest and highest salinities (squares). One exception is that the $\delta^{30}Si_{Si(OH)4}$ value of seawater endmember in the Amazon River Estuary is estimated based on a linear relationship between $\delta^{30}Si_{Si(OH)4}$ and $\ln(Si(OH)_4)$ (Fig. A5). In panels (b), (d), and (f), the error bars of the field $\delta^{30}Si_{Si(OH)4}$ data are the long-term external reproducibility of ±0.20‰ or the 2 standard deviations estimated from the repeated measurements if they are larger than ±0.20‰. The dashed lines above and below the corresponding solid line indicate errors deduced from the uncertainty in estimating the $\delta^{30}Si_{Si(OH)4}$ endmember values.

Figure 4. Dissolved inorganic nitrogen (DIN, nitrate plus nitrite) and dissolved inorganic phosphate (DIP) distributions along salinity gradients in the Amazon (a and b), Yangtze (c and d), and Pearl (e and f) River estuaries. The solid lines in each panel predict the conservative mixing for DIN or DIP between the river water and seawater endmembers, which are estimated according to field measurements at the lowest and highest salinities (squares). In panels (c) and (d), the

dashed lines and equations indicate the linear regression analysis for all data points over the entire salinity range.

Figure 5. Dissolved silicate ($Si(OH)_4$) concentrations and dissolved silicon isotopic compositions ($\delta^{30}Si_{Si(OH)4}$) distributions along salinity gradients in the Yangtze River Estuary in March 2012 (a and b) and July 2011 (c and d). Data were previously published in Zhang et al. (2015). The solid lines in each panel predict the conservative mixing for $Si(OH)_4$ or $\delta^{30}Si_{Si(OH)4}$ between the river water and seawater endmembers, which are selected according to field measurements at the lowest and highest salinities (squares). In panels (b) and (d), the error bars of the field $\delta^{30}Si_{Si(OH)4}$ data are the 2 standard deviations reported in Zhang et al. (2015). The dashed lines above and below the corresponding solid line indicate errors deduced from the uncertainty in estimating the $\delta^{30}Si_{Si(OH)4}$ endmember values, which is the long-term external reproducibility of ±0.10‰ for the Si isotope analyses in Zhang et al. (2015).

Figure 6. Monthly average wind velocity vectors around the Yangtze River Estuary in July 2011 (a), March 2012 (b), and March 2015 (c). The wind field is extracted from the reanalysis dataset of ERA-Interim (https://www.ecmwf.int/en/forecasts/datasets/archive-datasets/reanalysis-datasets/ era-interim).

884 **Figure 1**

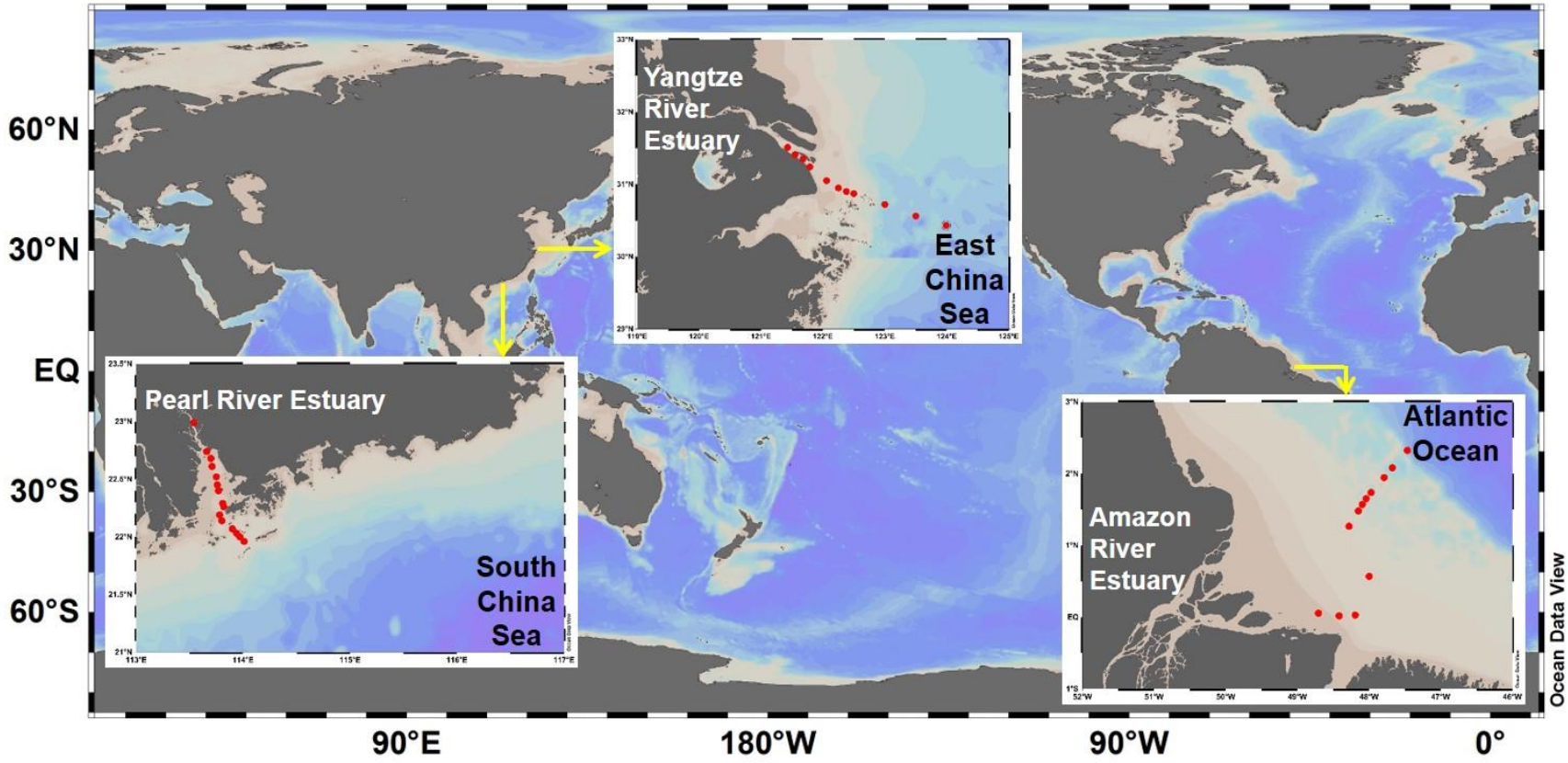

885

886 **Figure 2**

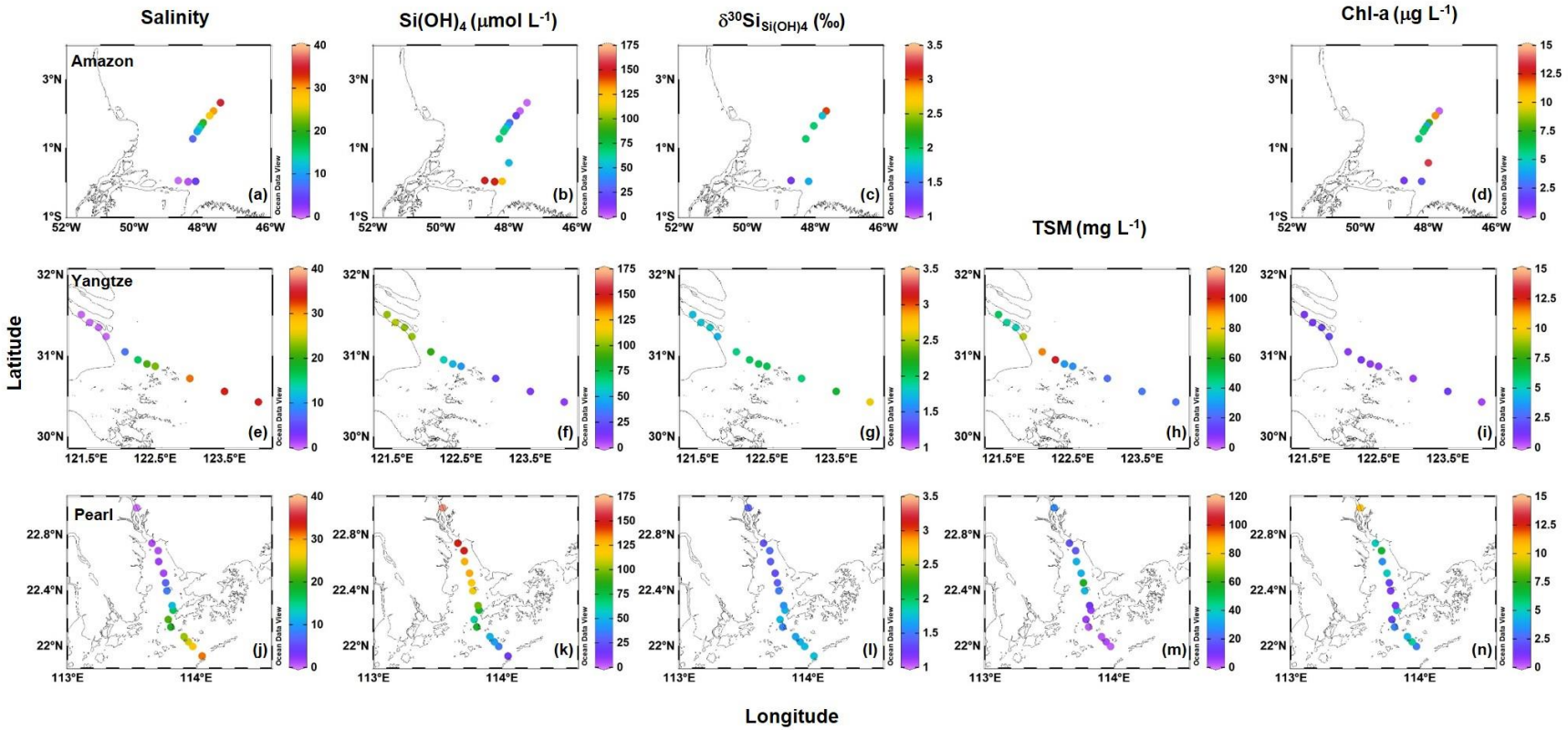

887

888 **Figure 3.**

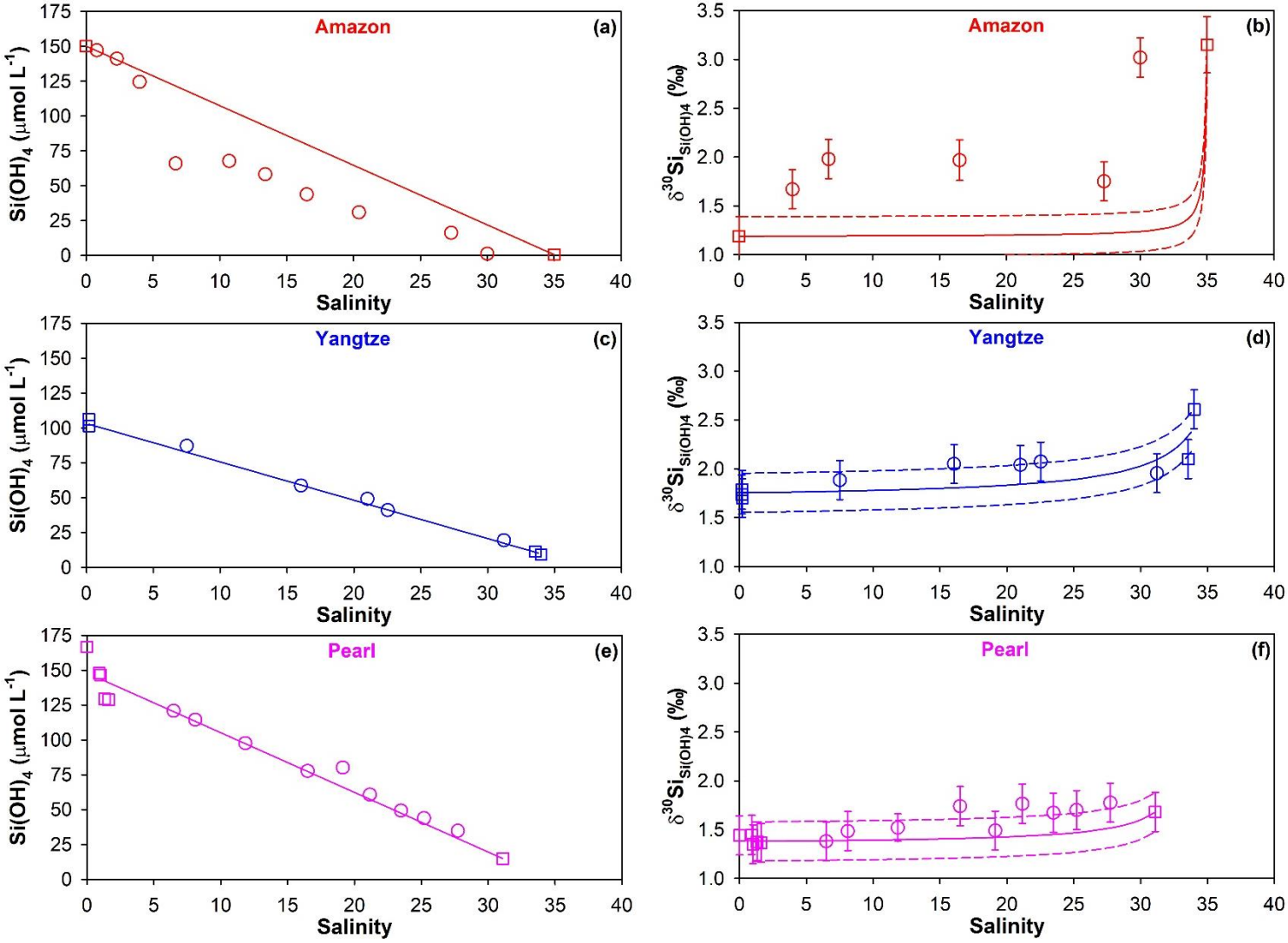

889

890 **Figure 4.**

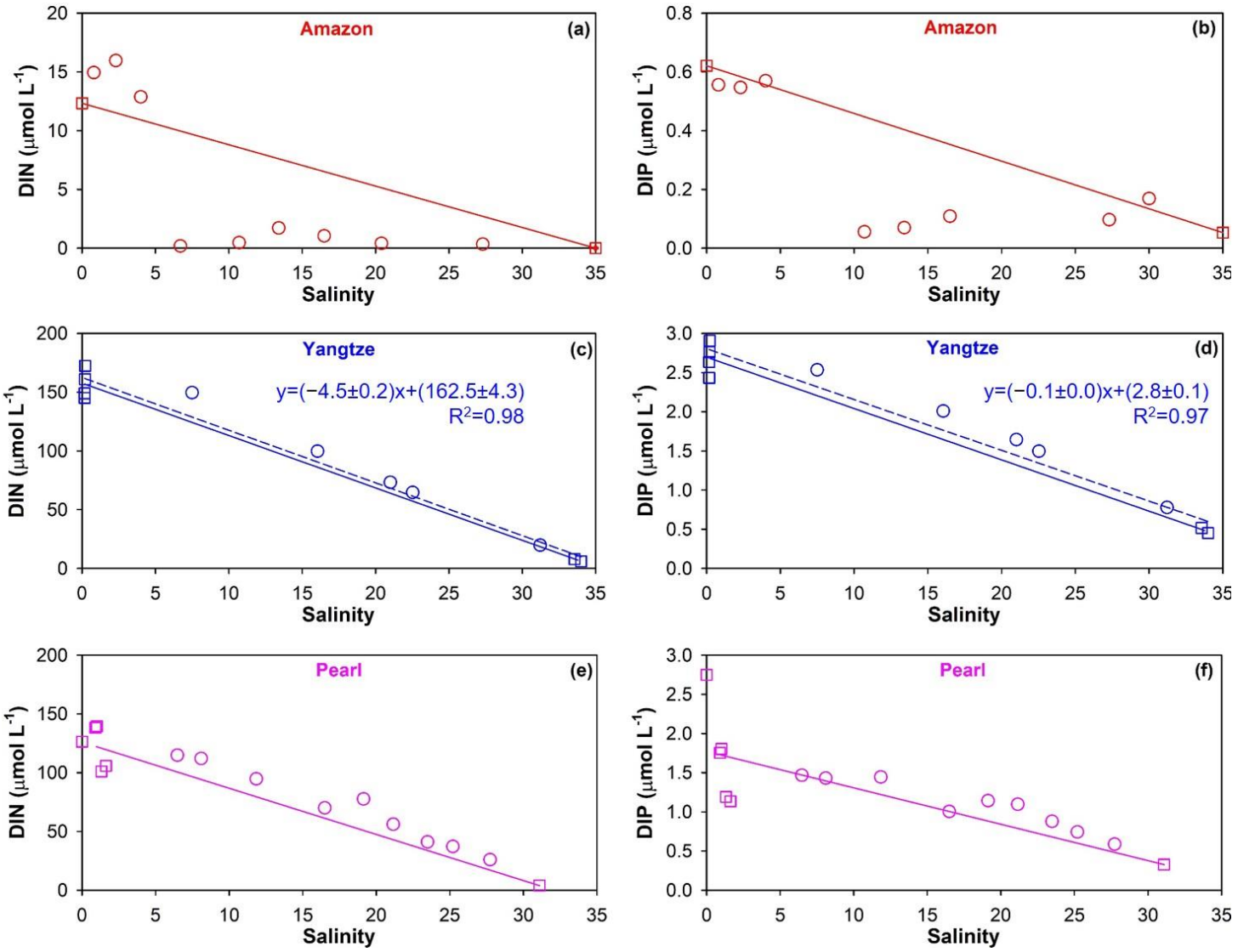

891

Figure 5.

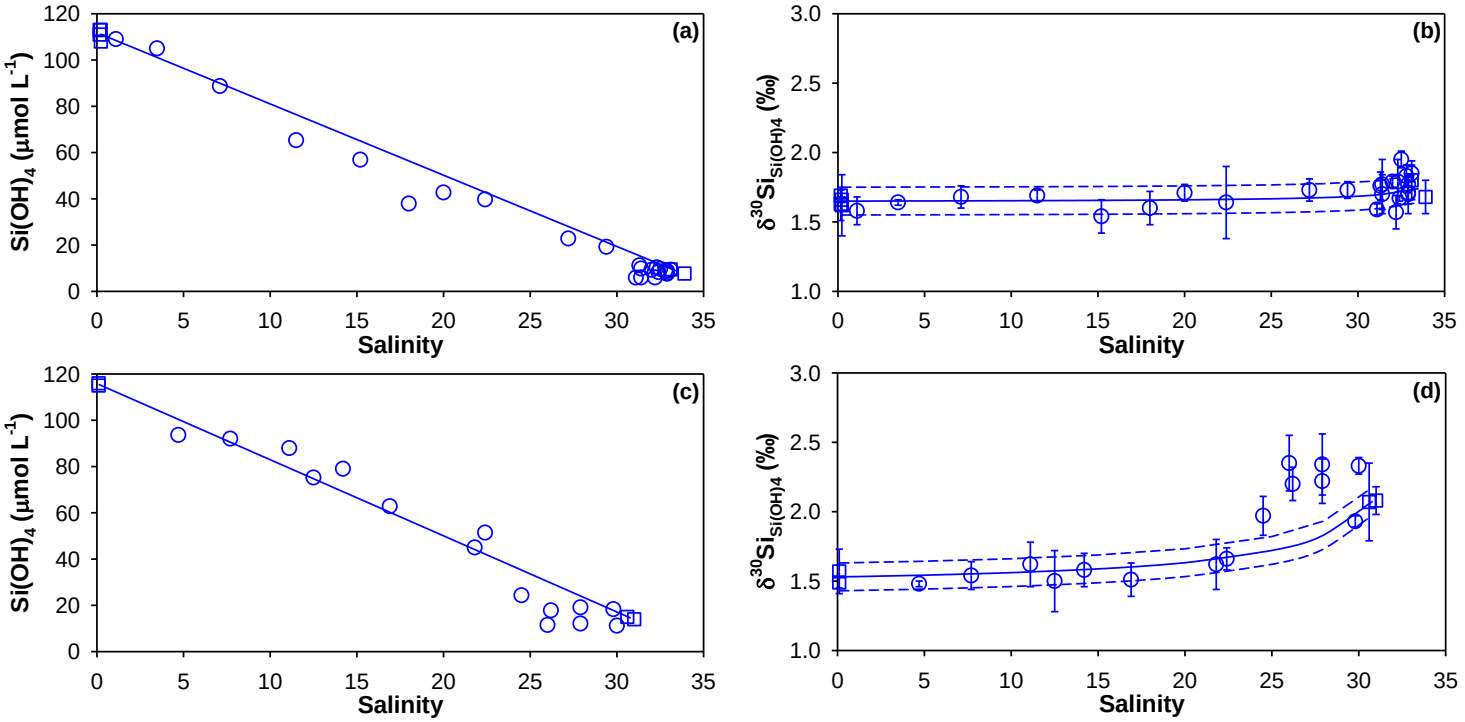

894 **Figure 6.**

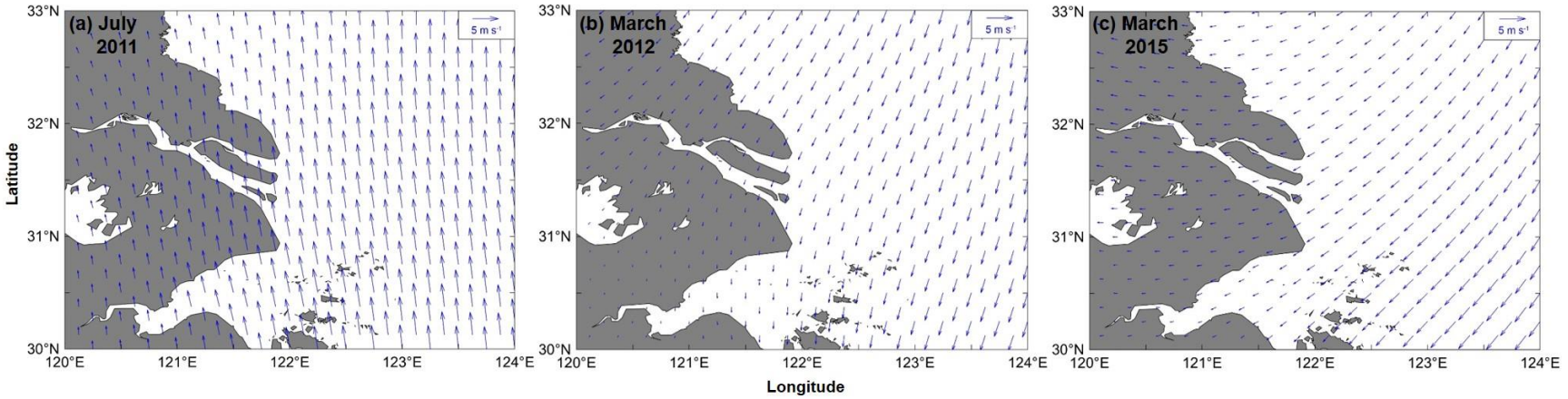

895